



HAL
open science

Study of the simultaneous Grinding/Ball-burnishing of AISI 4140 based on finite element simulations and experiments

Yasmine Charfeddine, Sawsen Youssef, Salem Sghaier, Jalila Sghaier, Hédi
Hamdi

► **To cite this version:**

Yasmine Charfeddine, Sawsen Youssef, Salem Sghaier, Jalila Sghaier, Hédi Hamdi. Study of the simultaneous Grinding/Ball-burnishing of AISI 4140 based on finite element simulations and experiments. International Journal of Mechanical Sciences, 2021, 192, pp.106097 -. 10.1016/j.ijmecsci.2020.106097 . hal-03493354

HAL Id: hal-03493354

<https://hal.science/hal-03493354>

Submitted on 17 Oct 2022

HAL is a multi-disciplinary open access archive for the deposit and dissemination of scientific research documents, whether they are published or not. The documents may come from teaching and research institutions in France or abroad, or from public or private research centers.

L'archive ouverte pluridisciplinaire **HAL**, est destinée au dépôt et à la diffusion de documents scientifiques de niveau recherche, publiés ou non, émanant des établissements d'enseignement et de recherche français ou étrangers, des laboratoires publics ou privés.



Distributed under a Creative Commons Attribution - NonCommercial 4.0 International License

1 Study of the simultaneous Grinding/Ball-burnishing of AISI 4140 2 based on finite element simulations and experiments

3 Yasmine Charfeddine^{1,3,*}, Sawsen Youssef¹, Salem Sghaier¹, Jalila Sghaier² and Hédi Hamdi³

4 1 University of Monastir, ENIM, LGM, Avenue Ibn El Jazzar, 5019 Monastir- Tunisia;
5 yasmine.charfeddine29@gmail.com; sawsen.youssef@gmail.com; salemsghaier@yahoo.fr

6 2 University of Monastir, ENIM, LTTPI, Avenue Ibn El Jazzar, 5019 Monastir- Tunisia;
7 jalila.sghaier@enim.rnu.tn

8 3 University of Lyon, ENISE, LTDS CNRS UMR 5513, 58 rue Jean Parot, 42023 Saint-Etienne – France;
9 hedi.hamdi@enise.fr

10 *Correspondence: yasmine.charfeddine29@gmail.com; Tel.: +216-92-730-635

11 Received: date; Accepted: date; Published: date

12 **Abstract:** In the manufacturing field, a growing interest is being held to the environment, to
13 sustainability and more precisely saving energy and time. Combining thermomechanical
14 with pure mechanical processes is an eco-friendly and profitable technique. In this paper, it
15 is proposed to combine grinding and ball-burnishing processes. Further from reducing time,
16 energy and cost of the manufacturing operations, this original combination is imagined to
17 take benefit from thermomechanical history occurring while grinding to optimise ball-
18 burnishing process in order to enhance the workpiece surface integrity. In this paper, the
19 impact of this newly developed process on the surface and subsurface behaviour is studied
20 through experiments and 3D FEM simulations. It is shown that performing simultaneously
21 grinding and ball-burnishing processes leads to a thick surface layer up to several
22 millimetres with compressive residual stresses state. This is an interesting result to increase
23 sustainability of metallic workpieces by enhancing wear resistance, fatigue strength and
24 fatigue lifetime.

25 **Keywords:** Thermo-mechanical process; Grinding; Ball-burnishing; 3D FEM Simulations;
26 Combined process; Hybrid process; Simultaneous grinding/ball-burnishing
27

28 1. Introduction

29 Grinding process is generally the final operation in the machining process procedure as
30 well as it is often considered as a finishing operation offering high dimensional precision,
31 geometrical shaping accuracy and good surface roughness [1,2]. Nevertheless, this abrasive
32 process can introduce some material deteriorations like microcracks formed at the surface and
33 below the ground zone [3,4] and also burning marks that can appear when reaching high
34 grinding temperature values [5-8]. Some other studies have shown that grinding can lead to
35 scratched and tore surface [9] probably caused by free abrasive grains, pulled off the grinding
36 wheel, in the grinding interface [10–12] or very high workpiece speeds [9]. Moreover,
37 grinding of hardened steel leads to tensile residual stress results at the surface and even
38 beneath it [13,14] that are known to be bad for fatigue resistance [15–19]. Burnishing process
39 is often launched after grinding to fix workpiece deteriorations caused by this
40 thermomechanical abrasive process [20,21].

41 Burnishing is a purely mechanical process capable of improving surface roughness by
42 pushing into the valleys the microscopic peaks left by the cutting tool on metals by applying a
43 pressure through a burnishing ball or roller. The surface obtained after burnishing has a
44 mirror like finish and is smoother [22–25] and harder [26–30]. Fatigue resistance of
45 mechanical components exposed to cyclic loads is enhanced too [31–35], thanks to the

46 appearance of compressive residual stresses [36,37]. These compressive residual stress results
 47 [38] reduce drastically the tensile stress values responsible for the emergence of the cracks
 48 and their propagation which enhances fatigue strength. Further, the plastic deformation [39]
 49 imposed by the pressure leads to strain hardening which has an impact on the workpiece
 50 microstructure [40,41] by refining the material grains beneath the surface [42].

51 Combining simultaneously grinding with ball-burnishing is a newly developed
 52 technique. It consists in grinding and burnishing performing together by placing the
 53 burnishing tool on the grinding machine and taking advantages of thermo-mechanical history
 54 of the workpiece initiated by the temperature changes occurring while grinding [43,44]. This
 55 hybrid manufacturing process ensures obtaining a better surface quality and durability while
 56 reducing manufacturing energy and time if compared to grinding and burnishing acting
 57 separately.

58 REGAL (French abbreviation of the combined Grinding Ball-burnishing process) is a
 59 promising process since it can enhance surface integrity like the combined turning/burnishing
 60 process in terms of surface roughness [45,46], hardness [45,47] and compressive residual
 61 stresses obtained on the top surface and subsurface [48]. Such surface integrity improvement
 62 increases wear resistance and fatigue life of workpiece. One of the main advantages of this
 63 simultaneous grinding/ball-burnishing process is the increase of the affected depth by
 64 compressive residual stresses compared to ordinary burnishing process.

65 The aim of this paper is to present an exploratory research study of the effectiveness of
 66 the newly developed technique combining grinding with ball-burnishing process. Researches
 67 are carried out by both experimentations and 3D FEM simulations using
 68 ABAQUS™/Standard.

69 2. Materials and experimental set-up

70 2.1. Materials

71 The workpiece material considered is the AISI 4140 and its chemical composition and
 72 thermo-mechanical behavior properties are resumed subsequently in Table 1 and Table 2.
 73 The burnishing ball is made of ceramic and is considered rigid for the rest of the study since
 74 its hardness is equal to 75HRC which is more important than the workpiece hardness, equal
 75 to 46HRC.

76 **Table 1.** Chemical compositions of AISI 4140.

Components	C	Si	Mn	P	S	Cr	Mo
Percent (%)	0.41	0.39	0.72	0.025	0.035	1.12	0.27

77 **Table 2.** AISI 4140 thermo-mechanical properties.

Young modulus [MPa]	210,000
Poisson's ratio ν	0.3
Density [Kg.m ⁻³]	7800
Thermal conductivity [mW.mm ⁻¹ .K ⁻¹]	46
Specific heat [mJ.t ⁻¹ .K ⁻¹]	477,000,000
Heat change coefficient [W.m ⁻² .K ⁻¹]	10 ⁵

78 2.2. Experimental set-up

79 The grinding machine used in this study is the ERNAULT-SOMUA FU-500 plane
 80 grinder and the burnishing tool used is a hydrostatic Ecoroll HG13 ball-burnishing tool. To

81 make possible the combined grinding and ball-burnishing processes simultaneously, the ball
82 burnishing tool is clamped to the grinding machine head using an aluminum fixing plate
83 (Figure 1). This plate replaces the actual cover of the grinding machine head and it is
84 designed and manufactured to suit the grinding machine used in this study.

85 The fixing plate is placed on the grinding machine using its two existing nuts and the two
86 clamps on both sides of the grinding machine to guarantee the stiffness of the fixing system
87 on the grinder head. Moreover, the ball-burnishing tool Ecoroll HG13 is placed in the center
88 of the aluminum plate and fastened to it using two U clamps and four nuts and bolts (Figure
89 1(b)). To ensure grinding and burnishing simultaneously, the ball-burnishing tool is placed
90 vertically in a plane parallel to the grinding wheel disk plane (Figure 1(b)). Further, centers of
91 the contact areas of the grinding wheel and the burnishing ball with the workpiece are in a
92 plane orthogonal to the manufactured workpiece surface containing the wheel center (Figure
93 1(b)). The “following system” existing in Ecoroll ball burnishing tools guarantees the ball to
94 be always in contact with the ground workpiece.

95 The performance of grinding and burnishing simultaneously occur when the workpiece is
96 placed under the grinding wheel and the ball-burnishing tool at the same time. The workpiece
97 is then moved forwards and backwards according to a precise cross feed f and at workpiece
98 speed V_w . The grinding machine table is equipped with a KISTLER 9257A force
99 dynamometer to register the resulting forces.

100

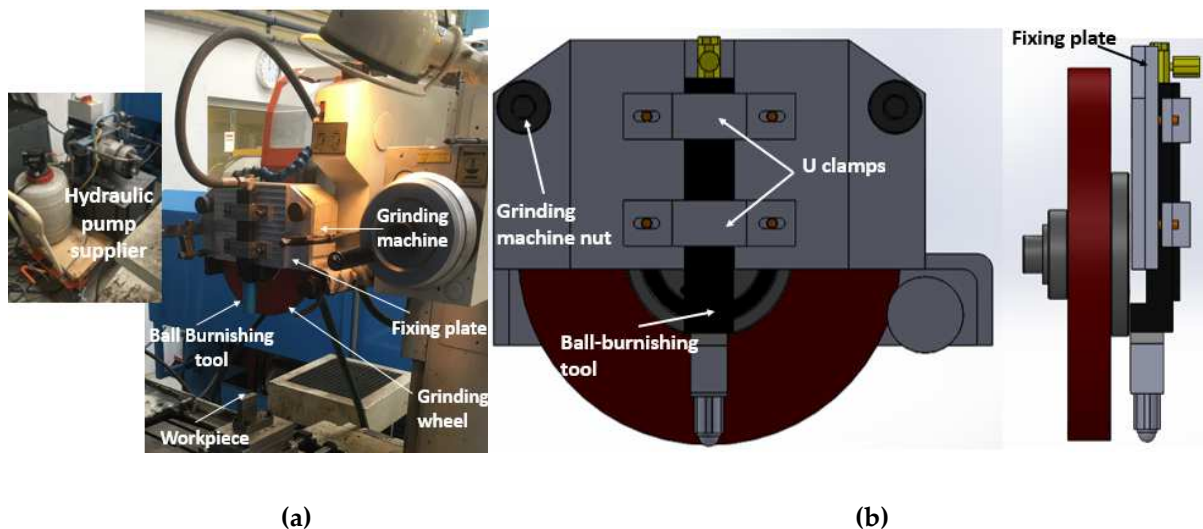


Figure 1. (a) Combined grinding/ball-burnishing setup; (b) SOLIDWORKS CAD front and side views of the burnishing tool assembly.

106 The abrasive tool is a type 1 CBN Wendt Boart grinding wheel 250-10-3-B126-RXJ75-
107 76.2. The main dimensions are 250 mm in diameter (D_s), 10 mm in width (b) and 3 mm CBN
108 layer. The burnishing tool used is a hydrostatic Ecoroll HG13 with a ceramic 13 mm diameter
109 burnishing ball controlled using an Ecoroll hydraulic pump supplier (Figure 1(a)). The
110 workpieces are extracted and manufactured from an AISI 4140 bar. The dimensions are 15
111 mm in width, 50 mm in length and a height of 50 mm.

112 2.3. Process conditions

113 The combined grinding/ball-burnishing process conditions are conducted for a workpiece
114 speed of $250 \text{ mm}\cdot\text{s}^{-1}$. The other grinding process conditions considered in this study are
115 shown in Table 3 and the other ball-burnishing process conditions are cited in Table 4. P
116 is the set hydraulic pressure supplied by the Ecoroll pump (Figure 1(a)).

117

118

Table 3. Grinding conditions.

Peripheral wheel speed	V_s [m.s ⁻¹]	37.5
Depth of cut	a_p [μm]	50
Workpiece speed	V_w [mm.s ⁻¹]	250

119

Table 4. Ball-burnishing conditions.

Burnishing ball diameter	d_b [mm]	13
Pressure	P [MPa]	30
Workpiece speed	V_w [mm.s ⁻¹]	250
Cross feed	f [mm]	1

120 3. Modelling and simulation

121 3.1. Modelling of grinding process

122

123

124

125

126

127

128

129

Grinding normal and tangential mechanical forces values are very low and the grinding cutting speeds are very high as compared to other material removing processes such as turning, milling and so on. Nevertheless, grinding power is high due to high grinding speed and it is assumed that all this power is converted as heat [2,6,49]. A fraction of this heat energy goes into the workpiece and involves thermomechanical phenomena because of the loading type, and the strain resulting from the thermal expansion. The rest of energy is dissipated through grinding micro-chips and environment.

130

131

132

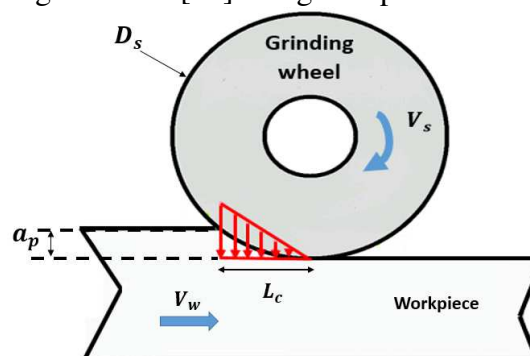
133

134

135

136

The grinding process is modeled as a moving heat source representing the action of the abrasive wheel on the workpiece surface (Figure 2). To quantify the input power, it is assumed that all the grinding power is sooner or later converted as heat in the manufacturing area [2,6,49]. Between 65% and 85% of the generated thermal power enter into the workpiece as heat [49–53]. Furthermore, many researchers demonstrated that the heat flux distribution in the grinding area is linearly arranged [43,54]. It is then said that the heat flux is modelled by a triangular moving heat flux [55] along the specimen's surface (Figure 2).



137

138

Figure 2. Triangular heat flux distribution.

139

140

141

142

143

144

In this paper the linear heat flux density is computed using Equation 1 as a function of the contact length l_c (Equation 2), the thermal power P_w entering into the workpiece, the active grinding wheel width b , and the curvilinear abscissa Y [43]. The thermal power P_w (Equation 3) is as well depending on the grinding tangential force F_t , the grinding wheel velocity V_s and the fraction ϵ of the total energy generated that really goes into the workpiece. In this paper, ϵ is taken equal to 75% [49].

$$q_w(Y) = \frac{2 \cdot P_w}{b \cdot l_c^2} \cdot Y; Y \in [0, l_c] \quad (1)$$

145 The contact between the grinding wheel and the workpiece (Figure 2) is defined by an arc
 146 circle. The length of this arc is defined as the grinding contact length l_c (Equation 2).

$$l_c = \sqrt{a_p \cdot D_s} \quad (2)$$

147 The thermal power P_w (Equation 3) entering the workpiece is the fraction ε of the total
 148 mechanical power generated in the grinding interface. Total mechanical power is the dot
 149 product of the grinding force vector by the speed vector that is finally equal to the product of
 150 the tangential force component F_t and the peripheral grinding wheel speed V_s .

$$P_w = \varepsilon \cdot F_t \cdot V_s \quad (3)$$

151 The grinding tangential force can be modeled as a function of the equivalent chip thickness
 152 h_{eq} considered for the contact surface between the grinding wheel and the workpiece
 153 (Equation 4) [43].

$$F_t = 20 \cdot b \cdot (h_{eq})^{0.615} \quad (4)$$

154 Where:

$$h_{eq} = a_p \cdot \frac{V_w}{V_s} \quad (5)$$

155 With Equations 1 to 5, it is possible to compute grinding heat flux density that goes into
 156 the workpiece (Table 5) for different workpiece speed values and according to the grinding
 157 conditions cited in Table 3.

158 **Table 5.** Data used to calculate the heat flux densities for different workpiece speed
 159 values.

V_w [mm.s ⁻¹]	$\frac{2 \cdot P_w}{b \cdot l_c^2}$ [W.mm ⁻³]
100	24.3
200	37.26
250	42.74
300	47.81
400	57.1
500	65.46

166 The heat flux trajectory for numerical simulations of the grinding process are represented in
 167 Figure 3. The cross-feed f (Figure 3) is imposed by the ball-burnishing process.
 168
 169

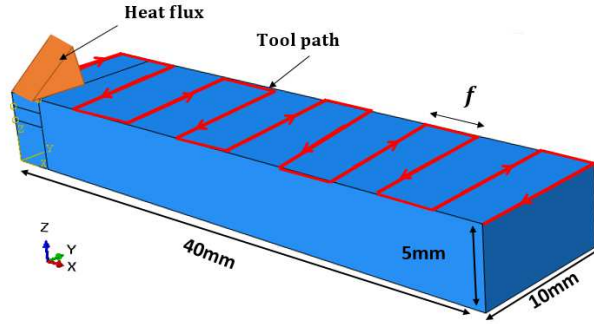


Figure 3. 3D model of step-cross grinding process.

170
171

172 3.2. Ball-burnishing process modelling approaches

173 The burnishing process can be modelled using two different manners. The first approach
174 consists in using the burnishing force when using the hydrostatic Ecoroll system used in this
175 study (Figure 4(a)). The ball-burnishing force is calculated from the hydraulic pressure P
176 (Figure 4(b)) that is assumed applied on the upper half sphere of the burnishing ball,
177 Equation 6. The other approach consists in applying to the ball the involved vertical
178 displacement δ (Figure 4(a)) resulting from the burnishing force.
179

$$F_b = \Pi R_{ball}^2 P \quad (6)$$

180

181 Where: R_{ball} is the burnishing ball radius.

182

183 In the case of the second approach, many research papers, modelled the ball-burnishing
184 process using a burnishing ball controlled by a vertical displacement corresponding to the
185 indentation depth δ (Figure 4(a)) [56, 57] calculated thanks to Hertz theory of contact
186 considered between two elastic solids (Figure 5). The Hertz theory of contact is only valid in
187 the elastic domain whereas burnishing process reaches the plastic domain. For this reason, to
188 study the relevance of using Hertz theory of contact, the calculated value of the vertical
189 displacement δ is compared to the numerical one obtained after indentation taking into
190 account the work hardening.

191

192 The computed ball-burnishing force using Equation 6 is different from the real force
193 applied on the 13 mm burnishing ball found experimentally for a set hydraulic pressure P of
194 30 MPa. This experimental ball-burnishing force measured by a KISTLER 9257A force
195 dynamometer is 25% lower than the calculated force. This can be due to the pressure loss
196 occurring in the gap between the ball and the burnishing tool socket (Figure 4(b)). Then, a
197 new relationship between the calculated and experimental ball-burnishing force is expressed
198 in Equation 7 and is in accordance with literature results [58].

$$F_{b, exp} = \frac{3}{4} F_b \quad (7)$$

199

200 The indentation numerical simulation is then launched using the experimental ball-
201 burnishing force of 2986 N found using Equation 7. The indentation simulation using the
202 experimental burnishing force permits to compare not only the penetration depth δ but also
203 other contact parameters given by Hertz theory of contact.

203

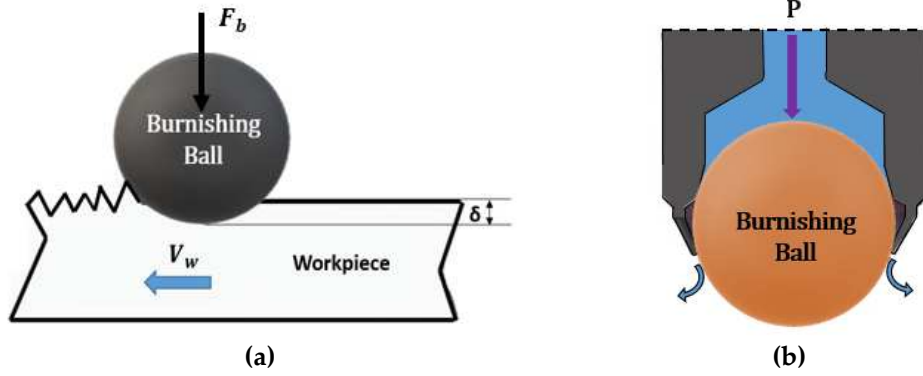


Figure 4. Ball-burnishing model for (a) an applied ball-burnishing force F_b or an applied vertical displacement δ ; (b) Illustration of the burnishing ball and ball retainer.

From Hertz elastic theory between a rigid sphere and a half-space (Figure 5) it is also possible to estimate the contact characteristics between the burnishing ball and the workpiece. One of them is the maximum contact pressure P_0 (Equation 8) between the burnishing ball and the workpiece when ball-burnishing force F_b is applied. Another one is the contact area and the last one is the indentation distance δ of the ball in the part calculated using Equation 9.

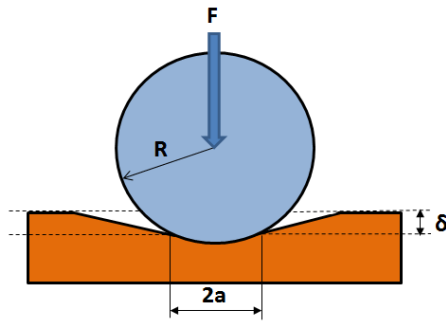


Figure 5. Illustration of Hertz elastic theory of contact.

The circular contact area diameter $2a$ is calculated using Equation 10, knowing that E^* (Equation 11) is the effective modulus, and R is the effective radius (Equation 12).

$$P_0 = \frac{3 F_b}{2 \pi a^2} \quad (8)$$

$$\delta = \frac{a^2}{R_{ball}} \quad (9)$$

$$2a = 2 \left(\frac{3 F_b R}{4 E^*} \right)^{\frac{1}{3}} \quad (10)$$

$$E^* = \left(\frac{1 - \nu_{workpiece}^2}{E_{workpiece}} + \frac{1 - \nu_{ball}^2}{E_{ball}} \right)^{-1} \quad (11)$$

$$\frac{1}{R} = \left(\frac{1}{R_{workpiece}} + \frac{1}{R_{ball}} \right) \quad (12)$$

The contact material properties of the workpiece and the burnishing ball used in this study are cited in Table 6.

220 **Table 6.** Mechanical and geometric properties related to Hertzian contact
 221 calculation.

$E_{\text{workpiece}}$ [MPa]	E_{ball} [MPa]	$\nu_{\text{workpiece}}$	ν_{ball}	E^* [MPa]	$R_{\text{workpiece}}$ [mm]	R_{ball} [mm]	R [mm]
210,000	315,000	0.3	0.26	137,111	∞	6.5	6.5

222
 223 The calculated Hertzian parameters for a pressure value of 30 MPa are presented in Table 7.

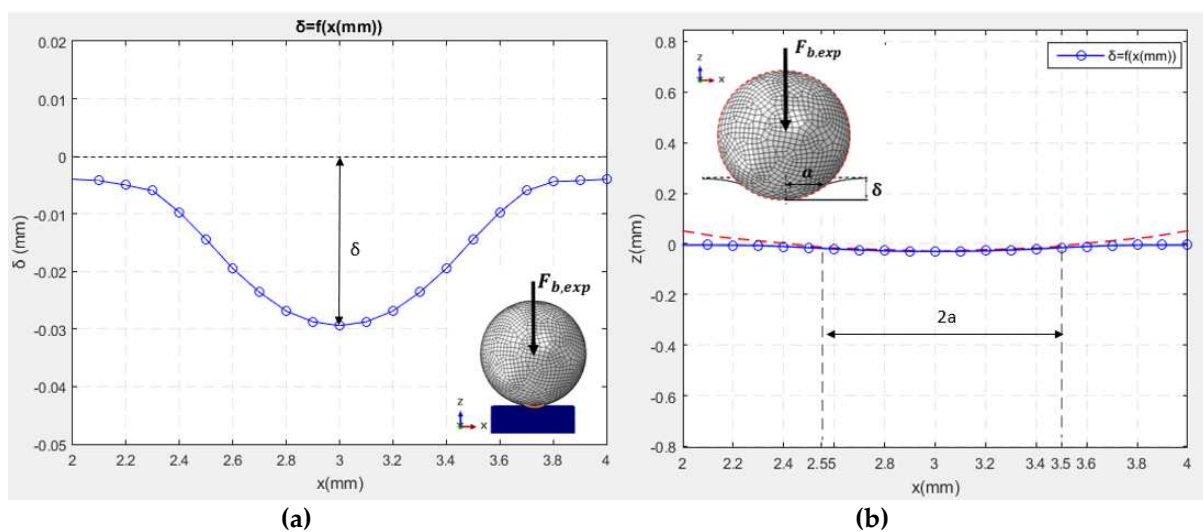
224 **Table 7.** Calculated Hertzian parameters for an applied hydraulic pressure of 30
 225 MPa.

P [MPa]	F_b [N]	$2a$ [mm]	P_0 [MPa]	δ [mm]
30	3,982	1.04	6,999	0.042

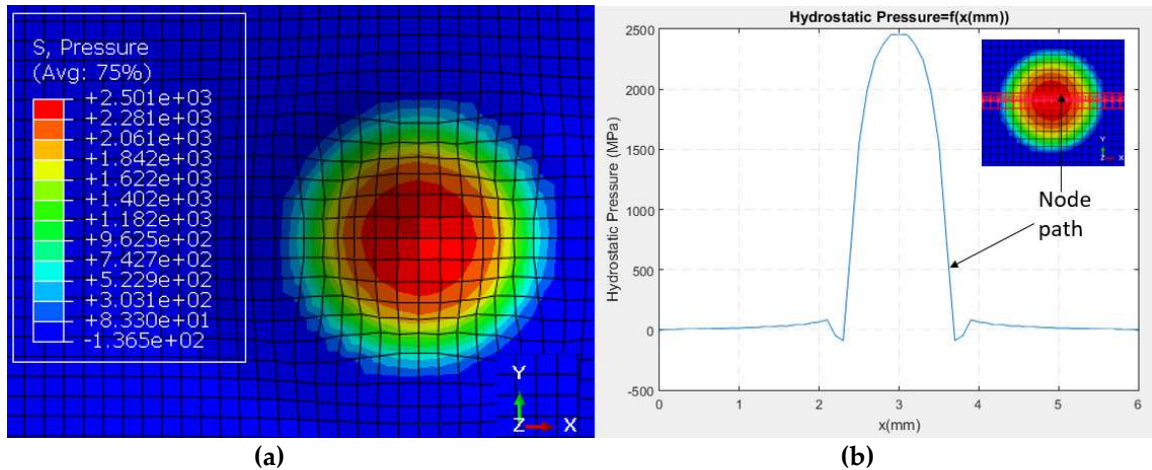
226
 227 The maximum indentation depth δ obtained numerically in Figure 6(a) is equal to
 228 0.029 mm and is 15% lower than the calculated value using Hertz theory of contact that is
 229 equal to 0.034 mm. In addition, the contact area diameter $2a$ found numerically in Figure 6(b)
 230 is equal to the calculated Hertzian value given in Table 8 and equal to 0.95 mm. In the other
 231 hand, Hertz theory of contact maximizes the contact pressure results P_0 equal to 6359 MPa
 232 calculated using Equation 8 as it is equal to 2456 MPa for the numerical simulations of
 233 indentation in Figure 7(a) and Figure 7(b). This difference can be explained by the fact that
 234 Hertz theory of contact is only valid in the elastic contact hypothesis and does not take into
 235 consideration the plastic deformation occurring.

236 From this comparative study, it is clear that the determination of the penetration depth δ
 237 by Hertz theory of contact is a poor approximation to simulate the burnishing process since it
 238 is overestimated by 15%. Using such penetration depth δ in burnishing process simulations
 239 involve an overestimation of the residual stress results obtained by burnishing.

240 To avoid further singularities related to the use of Hertz elastic theory of contact, the
 241 numerical simulations of the ball-burnishing process in this work are conducted using the
 242 experimental ball-burnishing force $F_{b, \text{exp}}$ instead of using the depth of penetration calculated
 243 using Hertz theory of elastic contact.
 244



245
 246 **Figure 6.** Numerical results of indentation using $F_{b, \text{exp}}$: (a) Indentation depth δ ; (b) circular
 247 contact area diameter between the burnishing ball and the workpiece.
 248



250
251
252
253

Figure 7. (a) Numerical hydrostatic pressure results after indentation; (b) Hydrostatic pressure curve along X-axis.

254
255

Table 8. Calculated Hertzian parameters versus numerical results after indentation for an applied ball-burnishing force of 2986 N.

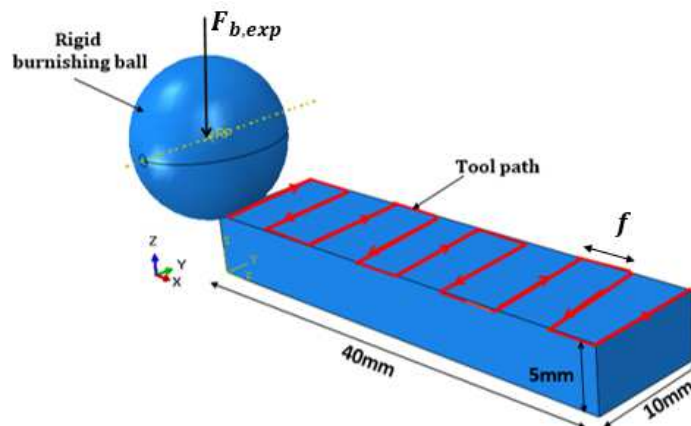
	$F_{b,exp}$ [N]	δ [mm]	2a [mm]	P_0 [MPa]
Hertz theory	2,986	0.034	0.95	6,359
FEM Analysis	2,986	0.029	0.95	2,456

256

257 *3.3. Adopted approach for modelling ball-burnishing process*

258 In the previous section, it has been demonstrated that using Hertz elastic theory of
259 contact is not adequate for the burnishing process since it does not take into account the work
260 hardening occurring while burnishing. The best way to model burnishing process is either to
261 launch an indentation study using the experimental burnishing force and taking into
262 consideration plasticity and then simulate the burnishing process using the value of the
263 vertical displacement found numerically or directly simulate the burnishing process using the
264 experimental burnishing force. In this study, the burnishing simulation adopted is using an
265 applied experimental burnishing force to avoid supplementary time by using two simulations
266 instead of one.

267 The ball-burnishing process is modeled by a rigid ball rolling on the workpiece surface at
268 the workpiece velocity V_w and on which an experimental burnishing force $F_{b,exp}$ is applied at
269 its center (Figure 8).



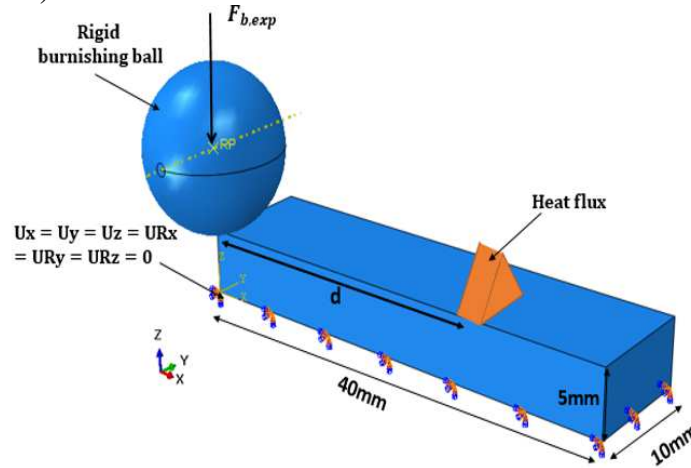
270

271

Figure 8. Ball-burnishing model.

272 *3.4. Modelling of combined grinding/ball-burnishing process*

273 The combined grinding/ball-burnishing process model consists in placing the burnishing
274 ball next to the triangular heat flux. The burnishing ball and the heat flux move forwards and
275 backwards along a predefined path and at the same speed equal to the workpiece speed V_w
276 (Figure 3 and Figure 9).



277
278

Figure 9. Combined grinding/ball-burnishing model.

279 The 3D model of combined grinding/ball-burnishing is considered thanks to the software
280 ABAQUS™/Standard. The implicit method of calculation is then chosen to simulate
281 especially material spring back in order to obtain the simulated residual stress.

282 Only a part of the experimental specimen with the dimensions of 40x10x5 mm³ (Figure
283 9) was considered in the numerical simulation in order to optimize the geometrical model and
284 to reduce simulations time. The workpiece is considered deformable with a Johnson-Cook
285 elasto-plastic constitutive law and is fixed at its bottom.

286 The Johnson-cook parameters used in this study for the AISI 4140 are in Table 9.

287 **Table 9.** Johnson-cook parameters for the AISI 4140 [59].

A[MPa]	B[MPa]	n	m
595	580	0.133	1.03

288

289 Where: A is the yield stress (MPa), B the hardening modulus (MPa), n is the work
290 hardening exponent and m the thermal softening coefficient.

291

292 Grinding is modeled by a moving heat flux along the workpiece surface following a step-
293 cross path (Figure 3). The shape distribution of the heat flux is considered triangular in the
294 grinding working interface where the initial workpiece temperature is 20°C and the
295 convective heat exchange coefficient is equal to 10⁵ W.m⁻².K⁻¹. Whereas, the ball-burnishing
296 process is modeled by a rigid ball free to rotate along the workpiece surface with an imposed
297 vertical force (along Z direction) applied to its center (Figure 9) and calculated using
298 Equation 7. The value of the ball-burnishing force applied to the burnishing ball considered
299 for the ball-burnishing conditions presented in Table 4 equal to 2986 N is validated thanks to
300 the normal experimental force obtained in the stabilized zone (Figure 10(b)).

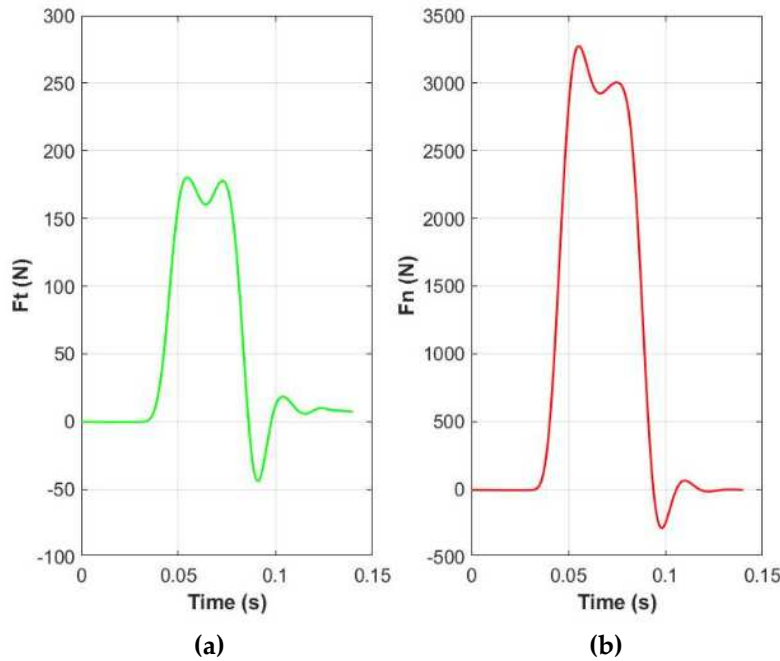
301

302 The simulation of the ball-burnishing process is composed of three steps: indentation,
 303 rolling and disengagement. The ball-burnishing boundary conditions vary according to the
 304 actual step used along the study and are summarized in Table 10.

305 **Table 10.** Boundary conditions of the burnishing ball.

Step	U1	U2	U3	UR1	UR2	UR3	Force
Indentation	0	0	free	0	0	0	$F_{b, exp}$
Rolling	*	*	free	free	free	free	$F_{b, exp}$
Disengagement	0	0	2 mm	0	0	0	0

306 * depends on the actual position of the ball along X and Y directions according to the predefined trajectory.



307
 308 **Figure 10.** (a) Experimental ball-burnishing tangential force results; (b) Experimental
 309 ball-burnishing normal force results.
 310

311 In order to estimate the right numerical coulomb friction coefficient proper to the ball-
 312 burnishing process, finite element residual stress results obtained for different friction
 313 coefficient are compared to the experimental residual stress results. The dynamic friction
 314 force F_t is composed of an adhesive force $F_{t,a}$ and a force related to the plastic deformation
 315 $F_{t,d}$ given by the Equation 13 [60].

$$F_t = F_{t,a} + F_{t,d} = (\mu_a + \mu_d) F_n \quad (13)$$

316 Where: μ_a is the adhesive friction coefficient and μ_d is the deformation friction
 317 coefficient.

318 The ABAQUS software permits introducing the Coulomb friction coefficient proper to
 319 purely friction. The Coulomb friction law becomes a poor approximation since there is an
 320 adhesive friction that needs to be considered. The friction coefficient obtained experimentally
 321 μ_{exp} includes the adhesive μ_a and deformation friction coefficient μ_d expressed in
 322 Equation 14. Therefore, from the numerical simulation it is possible to guess the adhesive
 323 coefficient by inserting the right coulomb friction value. To determine the adhesive

324 coefficient, the coulomb friction coefficient is changed until obtaining similar experimental
 325 and numerical residual stress curves.

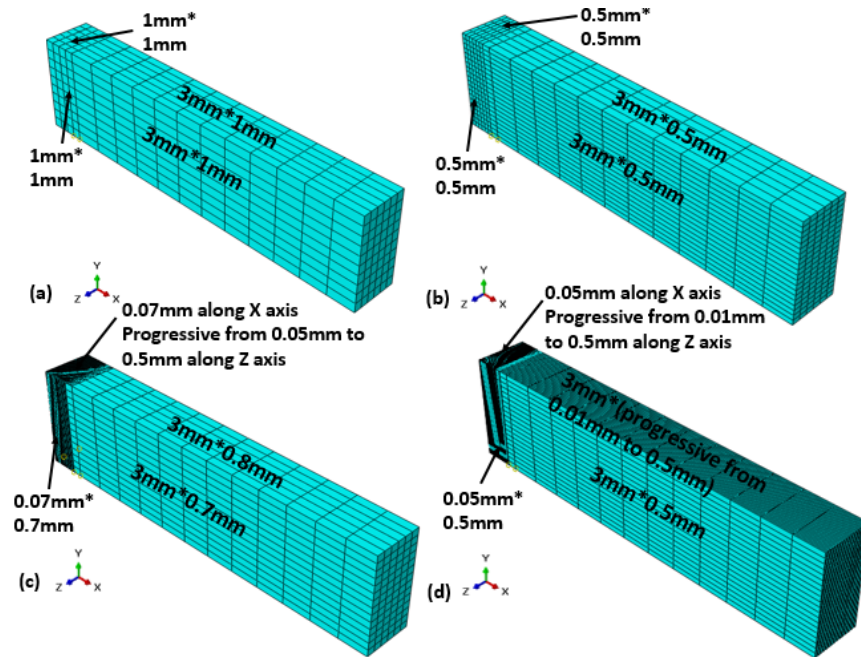
$$\mu_{exp} = \frac{F_t}{F_n} = (\mu_a + \mu_d) \quad (14)$$

326 Considering the experimental ball-burnishing force results given in Figure 10(a) and
 327 Figure 10(b), the calculated force ratio between the tangential ball-burnishing force F_t and the
 328 normal ball-burnishing force F_n mean values is equal to 0.06 which is the experimental value
 329 of the friction coefficient calculated in the stabilized zone.

330
 331 Combined grinding/ball-burnishing is a thermo-mechanical study so the mesh considered
 332 is type C3D8T. A refined mesh is adopted for a part of the workpiece ($3 \times 10 \times 5 \text{ mm}^3$) which is
 333 the interest zone presented in Figure 11. This precision of the mesh was chosen to see clearly
 334 the impact of this newly developed technique beneath the workpiece surface and reduce the
 335 calculation time by not considering a refined mesh for the total workpiece.

336 A study of mesh convergence of the workpiece was launched where different mesh sizes
 337 were considered (Figure 11). The choice of the adequate workpiece mesh was adopted based
 338 on two criteria. First criterion is that the mesh size along X-axis has to be lower than the cross
 339 feed f (1 mm) and the mesh size according to Y-axis has to be lower than the contact length
 340 between the workpiece and the grinding wheel l_c (3.5 mm) and at the same time lower than
 341 the contact area diameter between the burnishing ball and the workpiece $2a$ (0.95 mm). The
 342 second criterion is the report CPU time (Table 11).

343



344

345

346

Figure 11. Different workpiece mesh: (a) coarse mesh; (b) normal mesh; (c) optimal mesh;
 (d) very fine mesh.

347

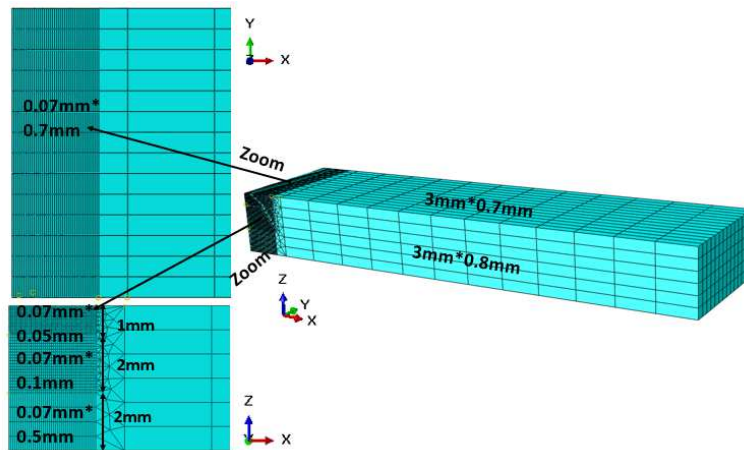
Table 11. Mesh strategy versus CPU time.

Mesh strategy	Illustration	CPU time
Coarse mesh size in the interest zone	Figure 11(a)	1 day
Normal mesh size in the interest zone	Figure 11(b)	3 days

Finer mesh size in the interest zone	Figure 11(c)	1 week
Very fine mesh size in the interest zone	Figure 11(d)	More than 2 weeks

348 The mesh strategy adopted in Figure 11(a) does not obey to the first criterion and the
349 mesh strategy adopted in Figure 11(b) gave results with a lack of precision if compared to
350 results obtained for the mesh strategy in Figure 11(c) and Figure 11(d). Further, no noticeable
351 changes in the output data are registered between the mesh strategy in Figure 11(c) and
352 Figure 11(d) except time CPU that is higher (Table 11).

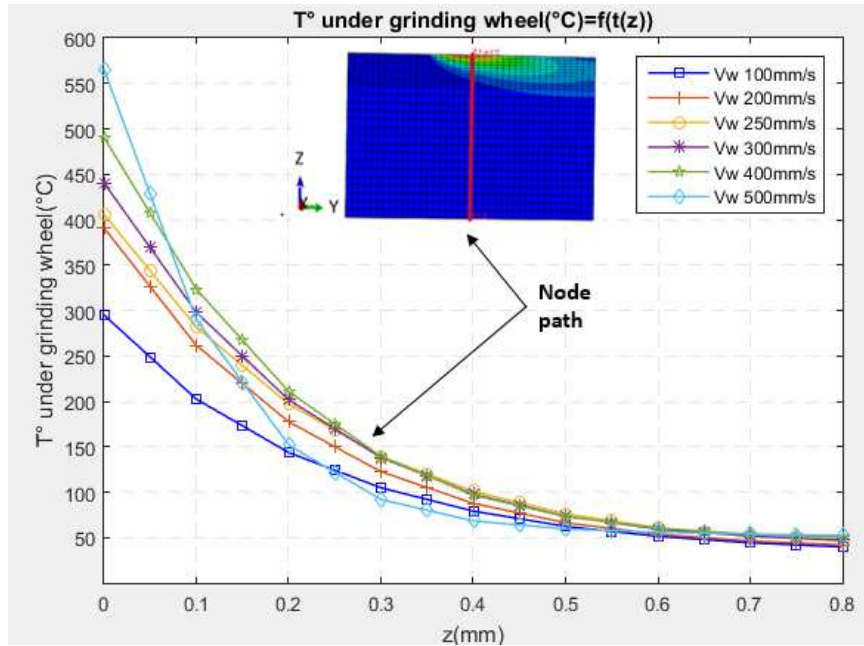
353 Since the precision of the results given by workpiece mesh in Figure 11(c) and Figure
354 11(d) are close, the adopted mesh in this study is the one illustrated the in Figure 11(c) with a
355 total of 26,962 elements and 30,058 nodes (Figure 12). This chosen mesh strategy permits to
356 gain in simulation time and ensures convergence of the model.



357 **Figure 12.** Adopted workpiece mesh.
358

359 3.5. Results

360 Simultaneous combined grinding/ball-burnishing consists in burnishing a pre-heated
361 surface by the grinding process. The effect of grinding temperature results is studied
362 numerically for different workpiece speeds V_w and cross feed values f (Figure 13 and Figure
363 14). The purpose behind this study is to maximize temperature results reached at the surface
364 and beneath it while burnishing. The temperature results according to the depth of the
365 workpiece are studied to optimize the grinding temperatures and choose the adequate
366 grinding parameters to consider in the combined grinding/ball-burnishing process.
367



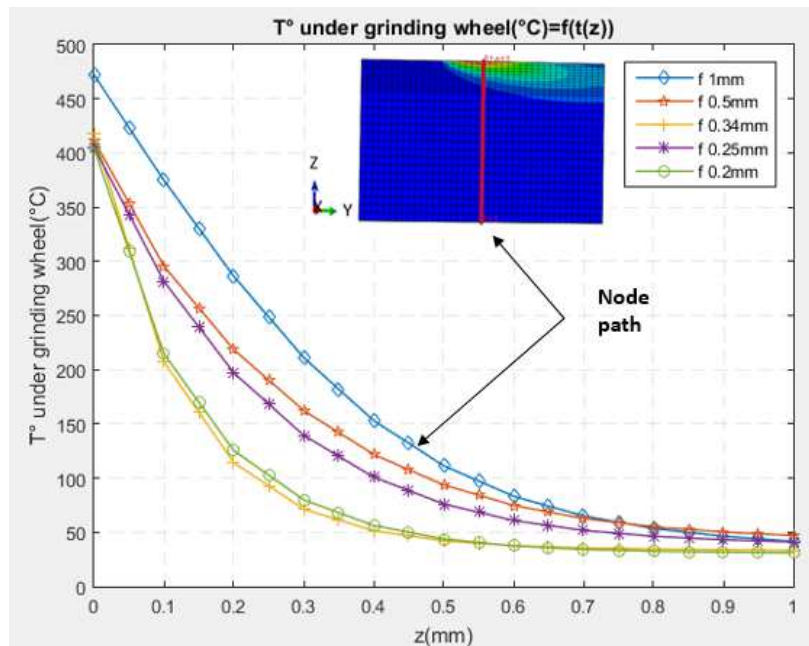
368
369
370
371

Figure 13. Effect of the workpiece speed on the numerical grinding temperature results along the workpiece depth for a cross feed of $f=0.25$ mm.

372
373
374
375
376
377
378
379
380
381
382
383

The highest temperature result at the workpiece surface is obtained for $V_w=500 \text{ mm.s}^{-1}$ and is equal to 565°C and the lowest equal to 295°C is obtained for $V_w=100 \text{ mm.s}^{-1}$ shown (Figure 13). The temperature of the workpiece surface increases when the workpiece speed increases. The more the workpiece speed increases, the more the heat flux density values increase, the more the temperature obtained at the surface are high.

Regardless of the cross-feed variations, the same heat flux densities are obtained since the cutting parameters (a_p, V_w, V_s) and the contact length l_c didn't change. When the cross-feed increases, the contact surface $S_c=f.l_c$ increases which leads to higher thermal power entering the workpiece which explains obtaining higher temperature results. As the surface of contact between the heat flux and the workpiece is the greatest for a cross-feed $f=1$ mm, the maximum temperature of about 470°C is then reached at the top surface (Figure 14).



384
385
386

Figure 14. Effect of the cross feed on the numerical grinding temperature results along the workpiece depth for $V_w=250 \text{ mm.s}^{-1}$ and $q_w(Y)=42.74 \text{ Y W.mm}^{-2}$.

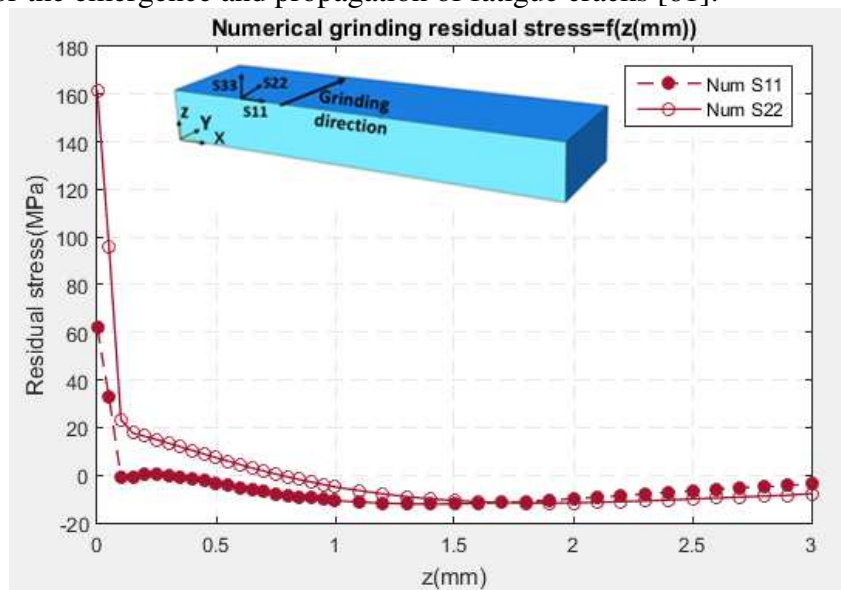
387
388
389
390
391
392
393
394
395

The grinding heat flux affects not only the workpiece surface, but heat generated also diffuses in the workpiece core, and leads to high temperature gradients up to different workpiece depths (Figure 13 and Figure 14). The temperature values reach 150°C at a depth of 0.4 mm of the workpiece for a cross-feed of 1 mm and $V_w=250 \text{ mm.s}^{-1}$ (Figure 14).

For the following numerical and experimental study of the combined grinding/ball-burnishing process, the experiments are launched at a workpiece speed of $V_w=250 \text{ mm.s}^{-1}$ and a cross feed of $f=1 \text{ mm}$ where high temperature values are reached while grinding.

396
397
398
399

After grinding, tensile residual stress are obtained in the grinding direction S22 and perpendicular to grinding direction S11 (Figure 15). These tensile residual stress results are known to be bad for the workpiece lifetime, wear and corrosion resistance since they are responsible for the emergence and propagation of fatigue cracks [61].



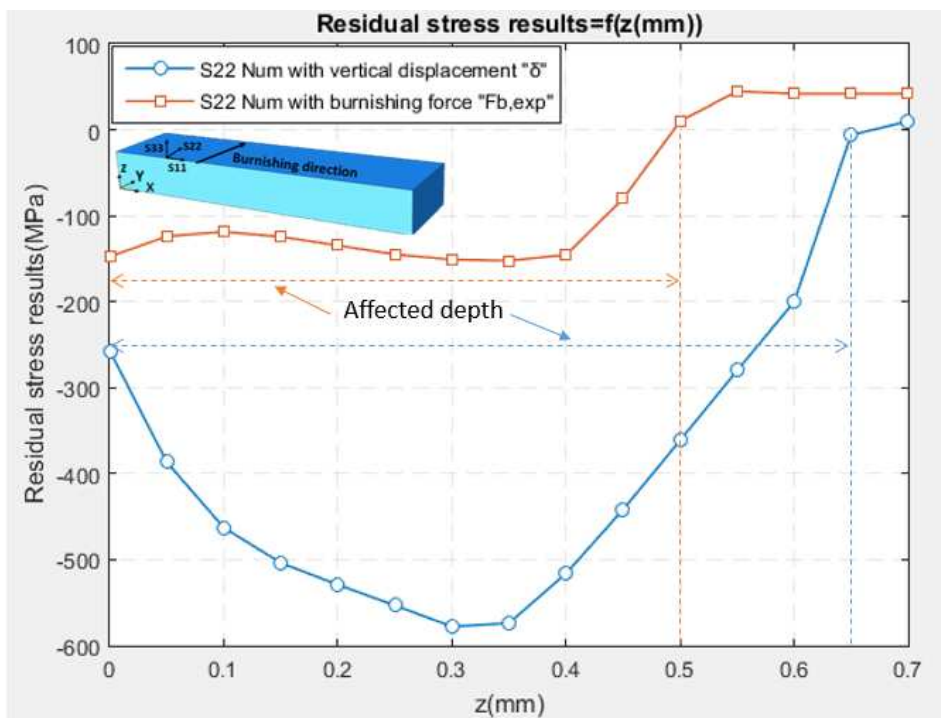
400

401
402
403

Figure 15. Numerical grinding residual stress results along the workpiece depth for a cross feed of $f=1\text{ mm}$, $V_w=250\text{ mm.s}^{-1}$ and $q_w(Y) = 42.74\text{ Y W.mm}^{-2}$.

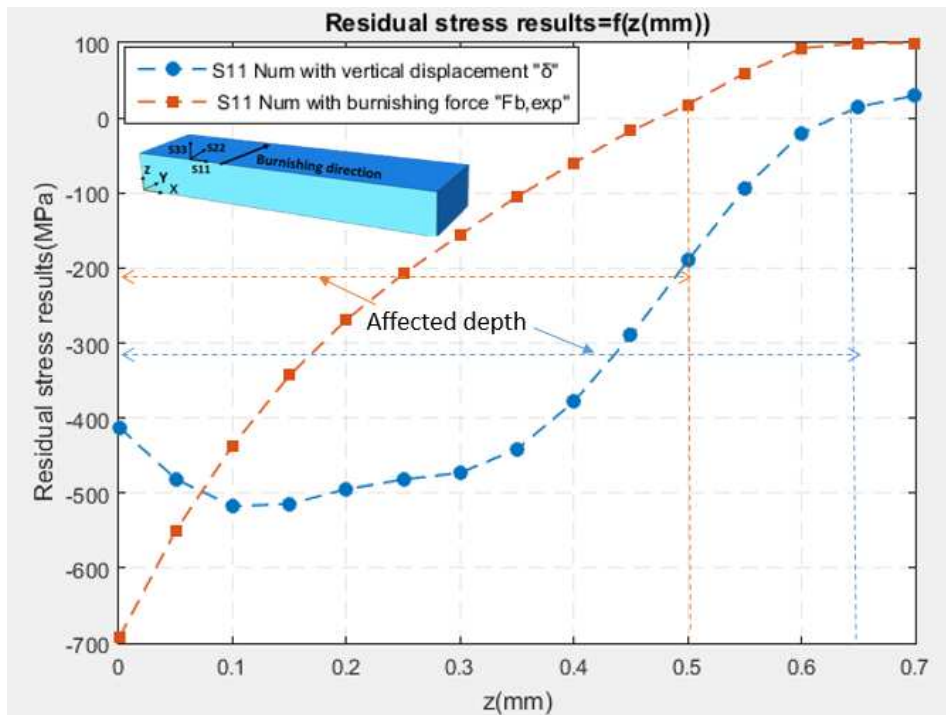
404
405
406
407
408
409
410
411
412
413
414
415
416
417
418
419
420
421
422
423
424
425
426

The modelling approach adopted for the ball-burnishing process has an impact on the residual stress obtained. As mentioned earlier in the modelling of ball-burnishing process section 3.2, two ways of modelling the ball-burnishing process are possible either applying a vertical displacement $\delta=0.034\text{ mm}$ calculated using Hertz theory of contact or applying the experimental value of the ball-burnishing force $F_{b,exp}=2986\text{ N}$ to the burnishing ball (Table 8). When comparing numerical residual stress obtained for those two types of modelling it is clear that there is a significant difference. The residual stress results are more compressive in the burnishing direction S22 for the imposed δ compared to the residual stress results obtained for an imposed ball-burnishing force (Figure 16). These compressive residual stress results in the burnishing direction S22 reach a value of -257 MPa at the surface and a maximum compressive value of -578 MPa at a 0.3 mm depth whereas the maximum value of the compressive residual stress result obtained when a ball-burnishing force is applied are equal to -147 MPa obtained at the top surface (Figure 16). Residual stress computed in the perpendicular to burnishing direction S11 are more compressive at the surface equal to -693 MPa when applying a ball-burnishing force, as they are equal to -412 MPa when imposing a vertical displacement to the burnishing ball (Figure 17). Moreover, the compressive residual stress layer reaches a more important depth equal to 0.65 mm when imposing a vertical displacement δ than when applying a ball-burnishing force with an affected depth of 0.5 mm (Figure 16). This can be explained by the fact that the indentation depth δ considered as vertical displacement calculated with Hertz theory of contact equal to 0.034 mm is higher than the indentation depth found numerically when imposing a ball-burnishing force equal to 0.029 mm (Figure 6(a)). Thus, higher indentation depth leads to higher compressive residual stress results at a more important workpiece depth.



427

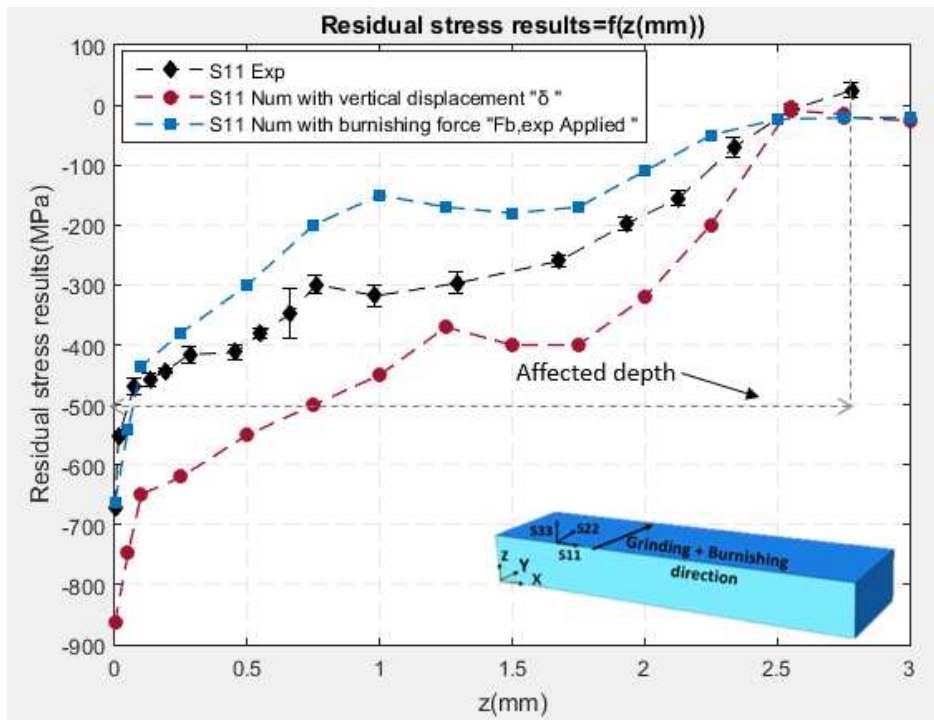
428 **Figure 16.** Numerical ball-burnishing residual stress results in the burnishing direction S22
 429 along the workpiece depth for an applied vertical displacement $\delta=0.034$ mm and a numerical
 430 ball-burnishing force $F_{b,exp}=2986$ N for $\mu=0.06$.



431
 432 **Figure 17.** Numerical ball-burnishing residual stress results perpendicular to burnishing
 433 direction S11 along the workpiece depth for an applied vertical displacement $\delta=0.034$ mm
 434 and a numerical ball-burnishing force $F_{b,exp}=2986$ N for $\mu=0.06$.

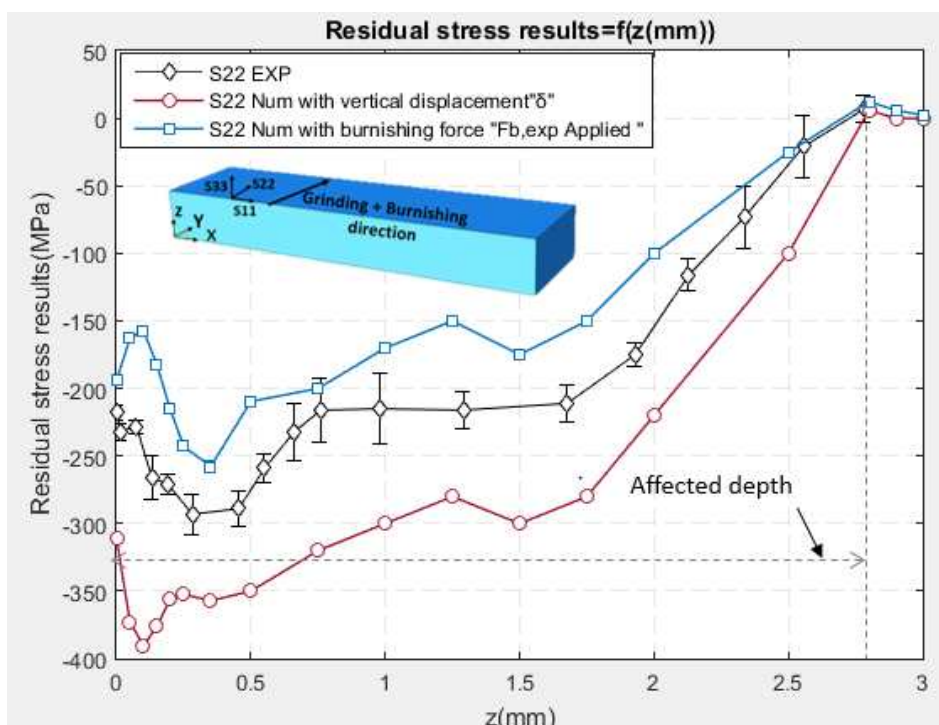
435
 436 Residual stress results obtained experimentally for the combined grinding/ball-
 437 burnishing process are compared to the numerical results obtained for both modelling
 438 approaches used to model the ball-burnishing process (Figure 18 and Figure 19). Residual
 439 stress results are more compressive at the top surface when numerical vertical displacement is
 440 adopted. These residual stresses can reach a value of -863 MPa in the perpendicular to
 441 grinding and burnishing direction S11 (Figure 18) and -311 MPa in the grinding and
 442 burnishing direction S22 (Figure 19). But residual stress profile at the top surface and beneath
 443 it for S11 and S22 when applying a ball-burnishing force are closer to the experimental
 444 results of the combined grinding/ball-burnishing. This led to the use of the imposed ball-
 445 burnishing force for the numerical simulation of ball-burnishing in the combined
 446 grinding/ball-burnishing process.

447
 448



449

450 **Figure 18.** Comparison between experimental and numerical REGAL residual stress results
 451 S11 (perpendicular to burnishing and grinding direction) using an applied vertical
 452 displacement $\delta=0.034$ mm and a numerical ball-burnishing force $F_{b,exp}=2986$ N and $\mu=0.06$.



453

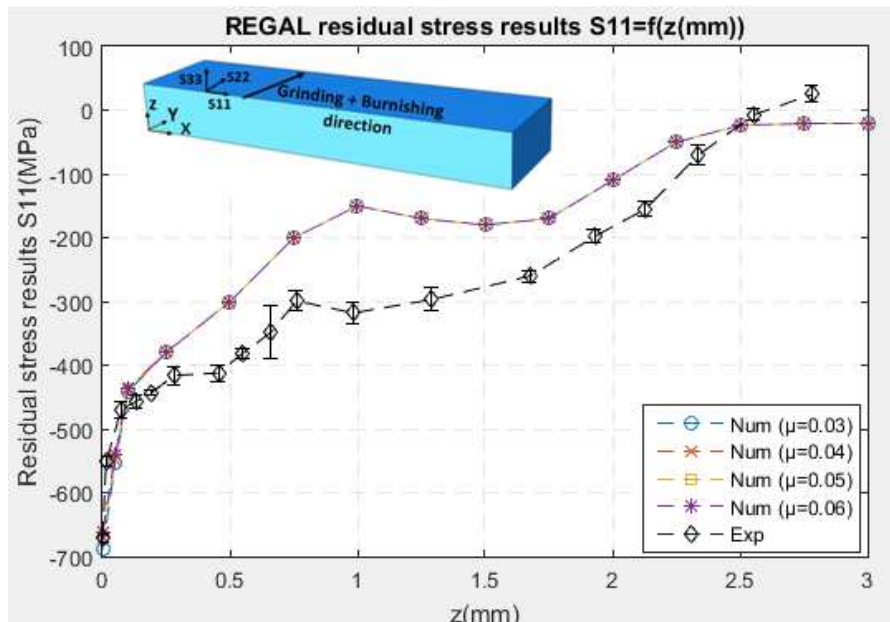
454 **Figure 19.** Comparison between experimental and numerical REGAL residual stress results
 455 S22 (in the burnishing and grinding direction) using an applied vertical displacement
 456 $\delta=0.034$ mm and a numerical ball-burnishing force $F_{b,exp}=2986$ N and $\mu=0.06$.

457 Different Coulomb friction coefficient values of $\mu=0.03$, 0.04, 0.05 and 0.06 where
 458 considered in the numerical simulation of the REGAL process using an imposed
 459 experimental ball-burnishing force applied to the burnishing ball modelling approach.

460 Residual stress results obtained numerically in the grinding and burnishing direction
 461 (S22) and perpendicular to them (S11) are compressive and in agreement qualitatively with
 462 the experimental curve obtained for the same operating conditions (Figure 20 and Figure 21).
 463 Furthermore, the same affected depth by the combined grinding/ball-burnishing equal to
 464 2.7 mm is obtained numerically and experimentally (Figure 20 and Figure 21). Maximum
 465 compressive residual stress results are obtained at the surface and decrease gradually beneath
 466 it according to the perpendicular direction to grinding and burnishing S11 (Figure 20).
 467 Whereas in the grinding and burnishing direction S22, the compressive residual stress results
 468 increase gradually in the subsurface until reaching a certain depth equal to 0.35 mm (Figure
 469 21).

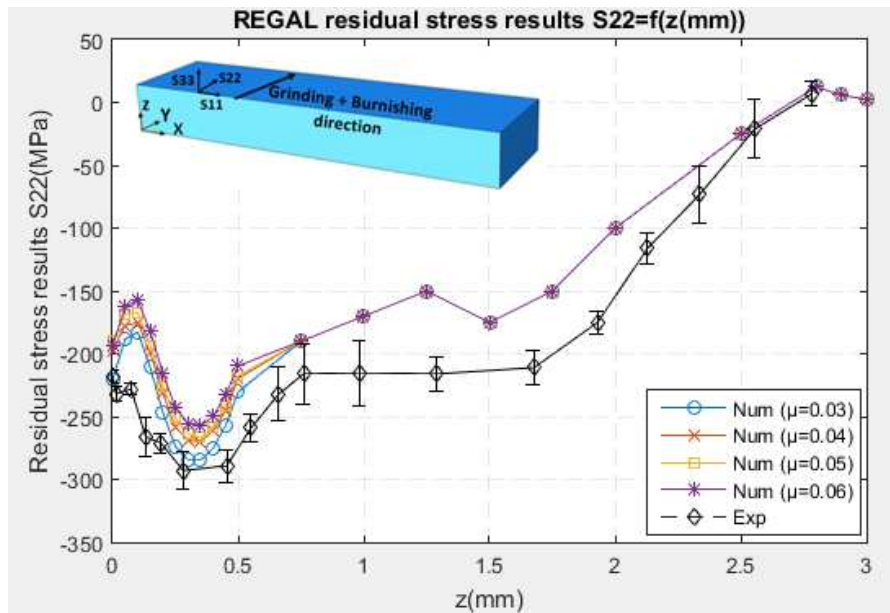
470 Residual stress profiles obtained numerically for several friction coefficients are
 471 perfectly superimposed on each other in the direction that is perpendicular to burnishing S11
 472 (Figure 20). Residual stress profiles in the grinding and burnishing direction S22 are slightly
 473 different for the four different friction coefficients and only for the first 0.75 mm depth of the
 474 specimen (Figure 21). These curves deviations are compared to experimental residual stress
 475 profiles (Figure 20 and Figure 21). At the surface, the residual stress results in the burnishing
 476 direction S22 for the friction coefficient values of 0.04, 0.05 and 0.06 are equal to -197 MPa.
 477 However, for a friction coefficient of 0.03, the residual stress value at the surface is equal to
 478 the experimental value of -218 MPa. Knowing that the force ratio between the tangential
 479 force F_t and the normal force F_n (Figure 10) is equal to 0.06. The approximation of the
 480 adhesive coefficient is then possible using Equation 14. Thanks to the adequacy between the
 481 experimental and numerical curve obtained for a friction coefficient of 0.03, the adhesive
 482 coefficient is then equal to 0.03.

483
 484



485
 486
 487 **Figure 20.** Comparison between numerical and experimental REGAL residual stress results
 488 S11 (perpendicular to the grinding/ball-burnishing direction) along the workpiece depth for
 489 different friction coefficient values, a cross feed of $f=1$ mm, $V_w=250$ mm.s⁻¹ and
 490 $F_{b, exp}=2986$ N.

491



492

493

494

495

496

Figure 21. Comparison between experimental and numerical REGAL residual stress results S22 (in the grinding/ball-burnishing direction) along the workpiece depth for different friction coefficient values, a cross feed of $f=1$ mm, $V_w=250$ mm.s⁻¹ and $F_{b,exp}=2986$ N.

497

498

499

500

501

502

503

504

505

506

507

508

509

510

511

512

513

514

515

516

517

518

519

520

521

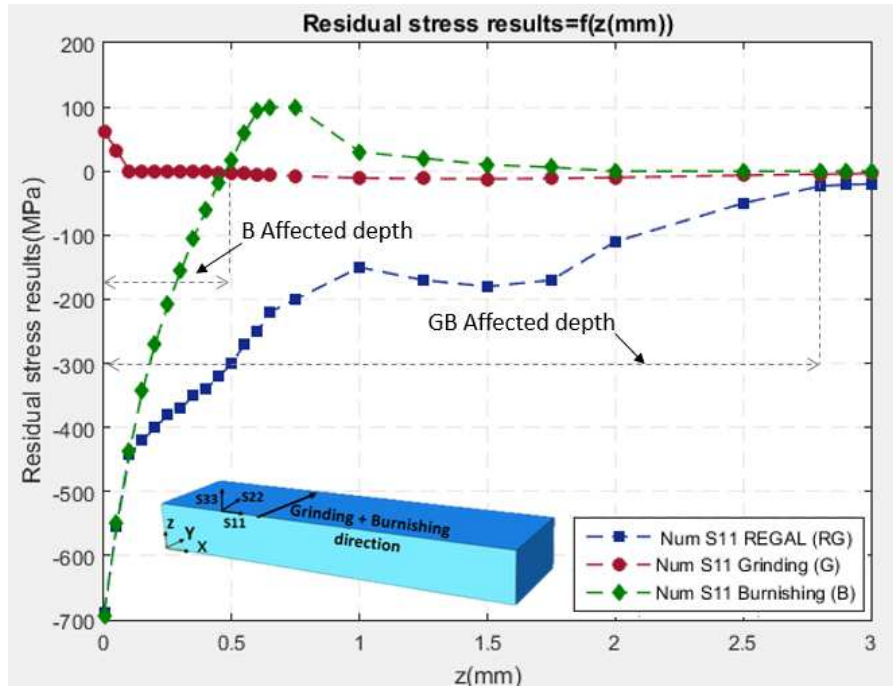
522

523

In order to analyze the effect of the newly developed technique involving grinding and ball-burnishing acting simultaneously, the residual stress results obtained by FE simulations are compared to those obtained numerically for grinding and ball-burnishing acting separately (Figure 22 and Figure 23). From these figures, it is seen that combining grinding with burnishing converts the tensile residual stresses obtained after grinding into compressive ones. These tensile residual stress results are equal to 161 MPa in the grinding direction S22 (Figure 23) and 62 MPa for the perpendicular to grinding direction S11 (Figure 22). The compressive residual stresses in perpendicular to grinding and burnishing direction S11 obtained at the surface reach values up to -693 MPa (Figure 22) for both REGAL and ball-burnishing process. On the other hand, REGAL process increases the compressive residual stresses results in the grinding and burnishing direction S22 if compared to the stress results obtained after the ball-burnishing process acting separately. Indeed, the compressive residual stress results at the surface increased from -147 MPa for the conventional ball-burnishing to -218 MPa for the combined grinding/ball-burnishing process (Figure 23). This can be interpreted by the fact that more mechanical working is induced when combining grinding with ball-burnishing process. Knowing that two mechanical loadings are involved in REGAL process one related to the thermo-mechanical loading relative to the grinding wheel and the other to the force applied to the burnishing ball.

The affected depth by the compressive residual stress results is more important for the combined process reaching 2.7 mm as it is only 0.5 mm for the regular ball-burnishing process (Figure 22 and Figure 23). This can be explained by the fact that in REGAL process, it seems that grinding temperature may activate for a sufficient duration a decrease of the mechanical behavior optimizing the ball-burnishing process leading to a deeper affected surface layer. The association of high temperature with high burnishing pressure leads to more mechanical working, which enhances compressive residual stress results at a more affected depth.

524



525

526

527

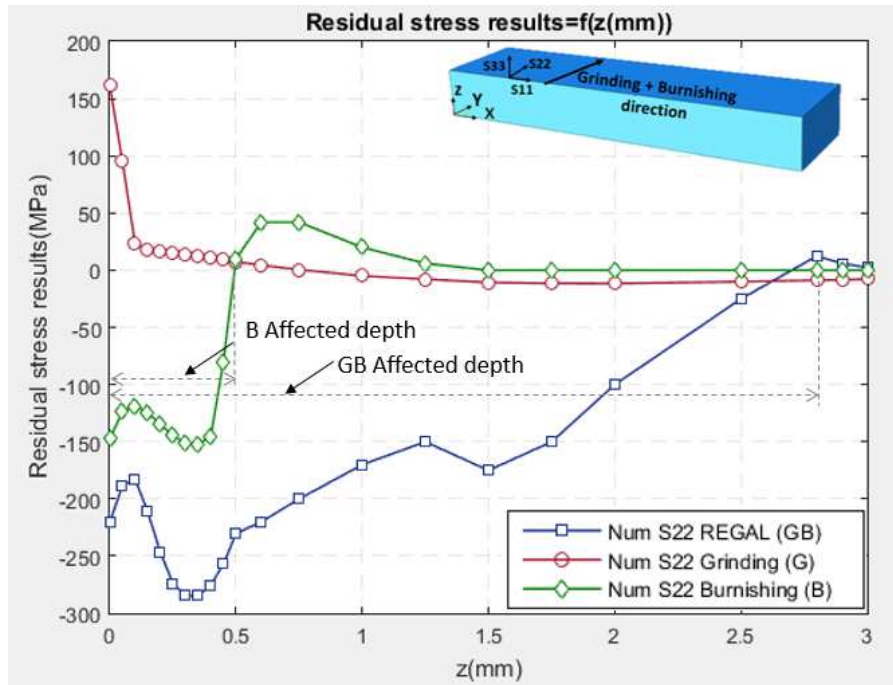
528

529

Figure 22. Numerical residual stress results S11 (perpendicular to the grinding/ball-burnishing direction) along the workpiece depth obtained for grinding (G), burnishing (B) and combined grinding/ball-burnishing (GB).

530

531



532

533

534

535

536

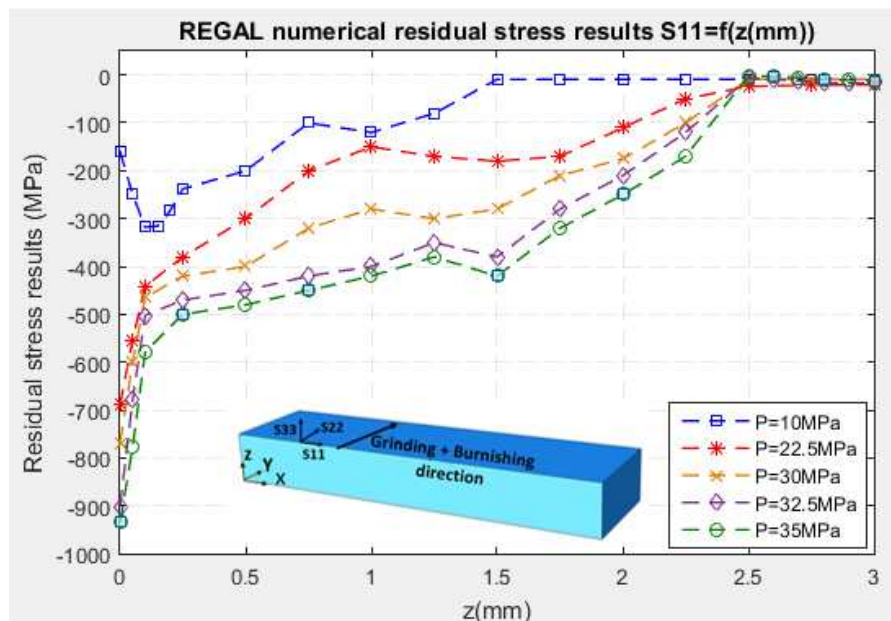
Figure 23. Numerical residual stress results S22 (in the grinding/ball-burnishing direction) along the workpiece depth obtained for grinding (G), burnishing (B) and combined grinding/ball-burnishing (GB).

537 To see the impact of the burnishing pressures on the residual stress state and the
 538 compressive affected depth by the combined grinding/ball-burnishing process, five different
 539 supply pressures were considered in the numerical study: 10 MPa, 22.5 MPa, 30 MPa, 32.5
 540 MPa and 35 MPa (Figure 24 and Figure 25). At the surface, the maximum compressive
 541 residual stress results are obtained for the maximum pressure of 35 MPa (Figure 24 and
 542 Figure 25) reaching a value of -934 MPa for S11 and -310 MPa for S22. Higher pressure
 543 values generate more compressive residual stress at the surface and beneath it and a more
 544 important compressive affected layer depth as reflected for the residual stress results S11
 545 (Figure 24). This would be the results of the increase in the burnishing ball penetration depth
 546 related to the increase of the ball-burnishing force applied to the rolling burnishing ball.

547 Tensile residual stress results in the burnishing direction S22 equal to 36 MPa are
 548 obtained for a pressure of 10 MPa (Figure 25). This can be explained by the fact that this
 549 pressure might not be sufficient to convert the grinding tensile residual stress results into
 550 compressive ones.

551 The affected depth by the combined grinding/ball-burnishing process is the same for the
 552 pressure values of 22.5 MPa, 30 MPa, 32.5 MPa and 35 MPa equal to 2.7 mm but this depth
 553 is equal to 1.75 mm for a pressure of 10 MPa (Figure 24 and Figure 25). According to these
 554 numerical results, the more the pressure increases, the more the affected depth increases but
 555 not infinitely since it is stabilized at 2.7 mm for a pressure of 22.5 MPa.

556

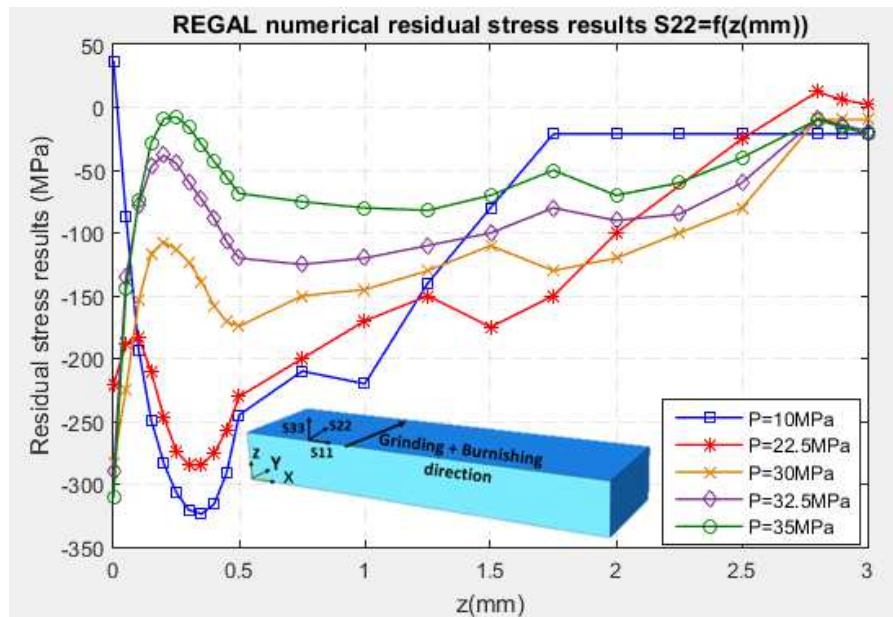


557

558

559 **Figure 24.** Impact of the burnishing pressure (P) on the numerical residual stress results S11
 560 perpendicular to grinding/ball-burnishing direction along the workpiece depth.

561



562
563
564
565

Figure 25. Impact of the burnishing pressure (P) on the numerical residual stress results S_{22} in the grinding/ball-burnishing direction along the workpiece depth.

566 Higher burnishing pressures lead to more compressive residual stress results at the
567 surface and reach a more important affected layer. This can be explained according to
568 Revankar et al. [62] that the increase of the ball-burnishing force applied to the burnishing
569 ball leads to an increase in the amount of plastic deformations involved and enhance the
570 hardness of the workpiece at an important workpiece depth.

571 Indeed, the temperature change under the ground surface and the plastic deformation
572 occurring with ball-burnishing acting simultaneously increase the depth of the plastically
573 deformed layer. The more the burnished depth increase the more the strain hardening
574 increase. Since while ball-burnishing, the material is deformed at a constant volume and the
575 surface deformation leads to its hardening which affects its subsurface by the same material
576 strain hardening circle.

577 The study of the effect of the pressure on the residual stress results leads to knowing that
578 there is a certain threshold value of the pressure. Starting from this pressure value, the
579 affected workpiece depth by the combined grinding/ball-burnishing process does not increase
580 and is stable for the current process manufacturing conditions to 2.7 mm.

581 Further, simultaneous grinding/ball-burnishing is a time effective process if compared to
582 thermochemical surface treatments such as nitriding that is a time-consuming process and
583 where the compressive residual stresses reach a depth of 0.1 mm for 36 hours of treatment
584 process [63].

585 4. Conclusions

586 In this present work, the thermal aspect of the grinding process was studied for different
587 workpiece speeds and cross feed values to optimize its thermal effect on the combined
588 grinding/ball-burnishing process. The ball-burnishing modelling approach based on applying
589 an experimental ball-burnishing force to the burnishing ball is adopted in this study since the
590 modelling approach using a vertical displacement based on Hertz theory of contact is not
591 adequate because it over estimates the indentation depth and further the residual stresses
592 values and profile. This ball-burnishing model chosen in this work was validated numerically
593 and experimentally. Furthermore, the numerical study of the combined grinding/ball-

594 burnishing process was conducted for different friction coefficient values and compared to
595 the experimental study for validation.

596 In addition, the comparison between combined grinding/ball-burnishing process with the
597 grinding and ball-burnishing processes acting separately permits to see the advantages of the
598 newly developed technique summarized as follows:

- 599 • Tensile residual stress obtained after grinding process became compressive thanks to
600 combining grinding/ball-burnishing process acting simultaneously.
- 601 • Compressive residual stress results after combined grinding/ball-burnishing process are
602 obtained in both directions and at a more important affected depth than the ball-
603 burnishing process acting separately.
- 604 • Combined grinding/ball-burnishing affects a more important workpiece depth (2.7 mm)
605 exceeding the depth obtained by thermo-chemical surface treatments.
- 606 • The increase of the burnishing pressure increases the compressive residual stress results
607 and ensures obtaining a deeper compressive layer. The affected depth is stable at a certain
608 pressure threshold value.

609
610 A thick layer of the compressive residual stress with small gradient are obtained when
611 grinding and ball-burnishing processes are exerted simultaneously. This might improve
612 workpiece resistance to environmental and mechanical external solicitations like severe
613 rolling contact or slip contact. Future study will focus on investigating the impact of the
614 burnishing pressure, the workpiece speed and the step over on the surface integrity of the
615 simultaneously ground/burnished workpiece.

616

617 **Acknowledgments:** The authors are grateful to the Program "Investissements d'Avenir"-
618 labelled by the French Government and operated by the National Research Agency (ANR) –
619 for financial support to the LabEx MANUTECH-SISE of Université de Lyon (France).

620 **References**

- 621 1. Mamalis, A. G.; Manolakos, D.; Markopoulos, A. P.; Kundrak, J. Thermal Modelling of
622 Surface Grinding Using Implicit Finite Element Techniques. *Adv. Manuf. Technol.*
623 **2003**, 21, 929–934. doi:10.1007/s00170-002-1410-3
- 624 2. Klocke, F.; Brinksmeier, E.; Weinert, K. Capability Profile of Hard Cutting and
625 Grinding Processes. *CIRP Ann. - Manuf. Technol.* **2005**, 54, 22–45. doi:10.1016/S0007-
626 8506(07)60018-3
- 627 3. Sanjay, A.; Rao, P.V. Experimental investigation of surface / subsurface damage
628 formation and material removal mechanisms in SiC grinding. *Int. J. Mach. Tools Manuf.*
629 **2008**, 48, 698–710. doi:10.1016/j.ijmachtools.2007.10.013
- 630 4. Zhang, J.; Yu, W.; Dong, E.; Zhang, Z.; Jiabin, S.; Gong, G. Study on grinding and
631 deformation fracture control of cold rolled titanium strip. *Metals.* **2020**, 10, 323.
632 doi:10.3390/met10030323
- 633 5. Youssef, S.; Ben Salem, W.; Brosse, A.; Hamdi, H. Residual stresses and metallurgic
634 transformations induced by grinding. *Int. J. Mach. Mach. Mater.* **2011**, 9, 223–232.
635 doi: 10.1504/IJMMM.2011.039648
- 636 6. Malkin, S.; Guo, C. *Grinding Technology, theory and applications of machining with*
637 *abrasives.* Industrial Press, New York. **2008**, second edition, 1–372, ISBN 978-0-8311-
638 3247-7
- 639 7. Malkin, S.; Guo, C. Thermal Analysis of Grinding. *CIRP Ann. - Manuf. Technol.* **2007**,
640 56, 760–782. doi:10.1016/j.cirp.2007.10.005

- 641 8. Wang, Z.; Yu, T.; Wang, X.; Zhang, T.; Zhao, J.; Wen, P.H. Grinding temperature field
642 prediction by meshless finite block method with double infinite element. *Int J Mech Sci.*
643 **2019**, 153–154, 131–142. doi:10.1016/j.ijmecsci.2019.01.037
- 644 9. Wenfeng, D.; Jiu Hua, X.; Zhenzhen, C.; Honghua, S.; Yucan, F. Grindability and
645 surface integrity of cast nickel-based superalloy in creep feed grinding with brazed CBN
646 abrasive wheels. *Chinese J. Aeronaut.* **2010**, 23, 501–510. doi:10.1016/S1000-
647 9361(09)60247-8
- 648 10. Suzuki, S.; Yoshihara, N.; Yan, J. W.; Kuriyagawa, T. High-Efficiency Mirror Grinding
649 of AlN by Ultra-Precision Plane Honing. *Key Eng. Mater.* **2007**, 329, 291–296.
650 doi:10.4028/www.scientific.net/kem.329.291
- 651 11. Demir, H.; Gullu, A.; Ciftci, I.; Seker, U. An investigation into the influences of grain
652 size and grinding parameters on surface roughness and grinding forces when grinding.
653 *Stroj. Vestnik/Journal Mech. Eng.* **2010**, 56, 447–454.
- 654 12. H. Sallem, H. Hamdi, Analysis of measured and predicted residual stresses by finishing
655 cylindrical grinding of high speed steel with CBN wheel. *Procedia CIRP.* **2015**, 31,
656 381–386.
- 657 13. Mamalis, A. G.; Kundrak, J.; Gyani, K. On the Dry Machining of Steel Surfaces Using
658 Superhard Tools. *Int. J. Adv. Manuf. Technol.* **2002**, 19, 157–162.
659 doi:10.1007/s001700200009
- 660 14. Ling, H. ; Yang, C.; Feng, S.; Lu, H. Predictive model of grinding residual stress for
661 linear guideway considering straightening history. *Int J Mech Sci.* **2020**, 176.
662 doi:10.1016/j.ijmecsci. 2020.105536
- 663 15. Yang, X.; Richard Liu, C.; Grandt, A. F. An Experimental Study on Fatigue Life
664 Variance, Residual Stress Variance, and Their Correlation of Face-Turned and Ground
665 Ti 6Al-4V Samples. *J. Manuf. Sci. Eng.* **2002**, 124, 809. doi:10.1115/1.1511174
- 666 16. Hashimoto, F.; Guo, Y. B.; Warren, A. W. Surface integrity difference between hard
667 turned and ground surfaces and its impact on fatigue life. *CIRP Ann. Manuf. Technol.*
668 **2006**, 55, 81–84. doi:10.1016/S0007-8506(07)60371-0
- 669 17. Rajasekaran, B.; Ganesh Sundara Raman, S.; Joshi, S. V.; Sundararajan, G. Effect of
670 grinding on plain fatigue and fretting fatigue behaviour of detonation gun sprayed Cu-
671 Ni-In coating on Al-Mg-Si alloy. *Int. J. Fatigue.* **2009**, 31, 791–796.
672 doi:10.1016/j.ijfatigue.2008.03.003
- 673 18. Guo, Y. B.; Warren, A. W.; Hashimoto, F. The basic relationships between residual
674 stress, white layer, and fatigue life of hard turned and ground surfaces in rolling contact.
675 *CIRP J. Manuf. Sci. Technol.* **2010**, 2, 129–134. doi:10.1016/j.cirpj.2009.12.002
- 676 19. Xu, R.; Zhou, Y.; Li, X.; Yang, S.; Han, K.; Wang, S. The effect of milling cooling
677 conditions on the surface integrity and fatigue behavior of the GH4169 superalloy.
678 *Metals.* **2019**, 9, 1179. doi:10.3390/met9111179
- 679 20. Bouzid Saï, W.; Saï, K. Finite element modeling of burnishing of AISI 1042 steel. *Int. J.*
680 *Adv. Manuf. Technol.* **2005**, 25, 460–465. doi:10.1007/s00170-003-1993-3
- 681 21. Dzierwa, A.; Markopoulos, A. P. Influence of ball-burnishing process on surface
682 topography parameters and tribological properties of hardened steel. *Machines.* **2019**, 7,
683 11. doi:10.3390/machines7010011
- 684 22. Grzesik, W.; Zak, K. Modification of surface finish produced by hard turning using
685 superfinishing and burnishing operations. *J. Mater. Process. Technol.* **2012**, 212, 315–
686 322. doi:10.1016/j.jmatprotec.2011.09.017
- 687 23. Zhang, T.; Bugtai, N.; Marinescu, I. D. Burnishing of aerospace alloy: A theoretical-
688 experimental approach. *J. Manuf. Syst.* **2015**, 37, 472–478.
689 doi:10.1016/j.jmsy.2014.11.004

- 690 24. Nestler, A.; Schubert, A. Roller burnishing of particle reinforced aluminium matrix
691 composites. *Metals*. **2018**, 8, 95. doi:10.3390/met8020095
- 692 25. Dzionk, S.; Scibiorski, B.; Przybylski, W. Surface texture analysis of hardened shafts
693 after ceramic ball burnishing. *Materials*. **2019**, 12, 204. doi:10.3390/ma12020204
- 694 26. El-Tayeb, N. S. M.; Low, K. O.; Brevern, P. V. Influence of roller burnishing contact
695 width and burnishing orientation on surface quality and tribological behaviour of
696 Aluminium 6061. *J. Mater. Process. Technol.* **2007**, 186, 272–278.
697 doi:10.1016/j.jmatprotec.2006.12.044
- 698 27. Korhonen, H.; Laakkonen, J.; Hakala, J.; Lappalainen, R. Improvements in the surface
699 characteristics of stainless steel workpieces by burnishing with an amorphous diamond-
700 coated tip. *Mach. Sci. Technol.* **2013**, 17, 593–610. doi:10.1080/10910344.2013.837351
- 701 28. Revankar, G. D.; Shetty, R.; Rao, S. S.; Gaitonde, V. N. Analysis of surface roughness
702 and hardness in ball burnishing of titanium alloy. *Meas. J. Int. Meas. Confed.* **2014**, 58,
703 256–268. doi:10.1016/j.measurement.2014.08.043
- 704 29. Teimouri, R.; Amini, S. Analytical modeling of ultrasonic surface burnishing process:
705 Evaluation of through depth localized strain. *Int J Mech Sci.* **2019**, 151, 118–132.
706 doi:10.1016/j.ijmecsci.2018.11.008
- 707 30. Rodríguez, A.; Calleja, A.; López de Lacalle, L.N.; Pereira, O.; González, H.; Urbikain,
708 G.; Laye, J.; Burnishing of FSWAluminum Al-Cu-Li components. *Metals*. **2019**, 9,
709 260. doi:10.3390/met9020260
- 710 31. Wierzchowski, D.; Ostertag, A.; Wagner, L. Fatigue Performance of the Mechanically
711 Sur 42CrMo4 and 54SiCr6: Shot Peening vs . Roller-Burnishing. *Icsp.* **2002**, 16–20,
712 468–473. doi:10.1002/3527606580.ch60
- 713 32. Nalla, R. K.; Altenberger, I.; Noster, U.; Liu, G.Y.; Scholtes, B.; Ritchie, R. O. On the
714 influence of mechanical surface treatments-deep rolling and laser shock peening-on the
715 fatigue behavior of Ti-6Al-4V at ambient and elevated temperatures. *Mater. Sci. Eng.*
716 **2003**, 355, 216–230. doi:10.1016/S0921-5093(03)00069-8
- 717 33. Majzoobi, G. H.; Zare Jouneghani, F.; Khademi, E. Experimental and numerical studies
718 on the effect of deep rolling on bending fretting fatigue resistance of Al7075. *Int. J. Adv.*
719 *Manuf. Technol.* **2016**, 82, 2137–2148. doi:10.1007/s00170-015-7542-z
- 720 34. Yuan, X.; Li, C. An engineering high cycle fatigue strength prediction model for low
721 plasticity burnished samples. *Int. J. Fatigue.* **2017**, 103, 318–326.
722 doi:10.1016/j.ijfatigue.2017.06.013
- 723 35. Fu, H.; Liang, Y. Study of the surface integrity and high cycle fatigue performance of
724 AISI 4340 steel after composite surface modification. *Metals*. **2019**, 9, 856.
725 doi:10.3390/met9080856
- 726 36. Maximov, J.; Anchev, A. P. Enhancement of fatigue life of rail-end-bolt holes by slide
727 diamond burnishing. *Eng. Solid Mech.* **2014**, 2, 247–264. doi:10.5267/j.esm.2014.7.001
- 728 37. Sanchez, L. E. A.; Giaretta, F.; Nogueira, L. G.; Neto, R. R. I. Effect of Hot Burnishing
729 Aided by Infrared Radiation on the Modification of Surface and Subsurface of AISI
730 1045 Steel. *Procedia CIRP.* **2017**, 58, 463–468. doi:10.1016/j.procir.2017.03.254
- 731 38. Lim, A.; Castagne, S.; Cher, W. C. Effect of Deep Cold Rolling on Residual Stress
732 Distributions Between the Treated and Untreated Regions on Ti – 6Al – 4V Alloy. *J.*
733 *Manuf. Sci. Eng.* **2017**, 138, 1–8. doi:10.1115/1.4033524
- 734 39. Grochała, D.; Berczyński, S.; Grządziel, Z. Modeling of burnishing thermally
735 toughened X42CrMo4 steel with a ceramic ZrO2ball. *Arch. Civ. Mech. Eng.* **2017**, 17,
736 1011–1018. doi:10.1016/j.acme.2017.04.009
- 737 40. Gharbi, F.; Sghaier, S.; Al-Fadhalah; K. J.; Benameur, T. Effect of ball burnishing
738 process on the surface quality and microstructure properties of aisi 1010 steel plates. *J.*
739 *Mater. Eng. Perform.* **2011**, 20, 903–910. doi:10.1007/s11665-010-9701-6

- 740 41. Fu, C. H.; Sealy, M. P.; Guo, Y. B.; Wei, X. T. Austenite-martensite phase
741 transformation of biomedical Nitinol by ball burnishing. *J. Mater. Process. Technol.*
742 **2014**, 214, 3122–3130. doi:10.1016/j.jmatprotec.2014.07.019
- 743 42. Baland, P.; Tabourot, L.; Degre, F.; Moreau, V. An investigation of the mechanics of
744 roller burnishing through finite element simulation and experiments. *Int. J. Mach. Tools*
745 *Manuf.* **2013**, 65, 29–36. doi:10.1016/j.ijmachtools.2012.09.002
- 746 43. Hamdi, H.; Zahouani, H.; Bergheau, J. M. Residual stresses computation in a grinding
747 process. *J. Mater. Process. Technol.* **2004**, 147, 277–285. doi:10.1016/S0924-
748 0136(03)00578-8
- 749 44. Zhang, Z. Y.; Shang, W.; Ding, H. H.; Guo, J.; Wang, H. Y.; Liu, Q. Y.; Wang, W. J.
750 Thermal model and temperature field in rail grinding process based on a moving heat
751 source Thermal model and temperature field in rail grinding process based on a moving
752 heat source. *Appl. Therm. Eng.* **2016**, 106, 855–864.
753 doi:10.1016/j.applthermaleng.2016.06.071
- 754 45. Shirsat, U. M.; Ahuja, B. B. Parametric analysis of combined turning and ball
755 burnishing process. *Indian J. Eng. Mater. Sci.* **2004**, 11, 391–396.
- 756 46. Mezlini, S.; Mzali, S.; Sghaier, S.; Braham, C.; Kapsa, P. Effect of a combined
757 machining/burnishing tool on the roughness and mechanical properties. *Lubr. Sci.* **2014**,
758 26, 175–187. doi:10.1002/lis.1239
- 759 47. Chaudhari, P.; Awari, G. K.; Khandare, S. S. Investigation of effectiveness of combined
760 turning and burnishing operations performed on lathe machine on an aluminium alloy
761 for the modification of surface texture. *Int. J. of Eng. Sci. Inv. Res. Dev.* **2015**, I, 1316–
762 1320.
- 763 48. Rami, A.; Gharbi, F.; Sghaier, S.; Hamdi, H. Some insights on Combined Turning-
764 Burnishing (CoTuB) process on workpiece surface integrity. *Int. J. Precis. Eng.*
765 *Manuf.* **2018**, 19, 67–78. doi:10.1007/s12541-018-0008-0
- 766 49. Kohli, S.; Guo, C.; Malkin, S. Energy Partition to the Workpiece for Grinding with
767 Aluminum Oxide and CBN Abrasive Wheels. *ASME J. Eng. Ind.* **1995**, 117, 160–168.
768 doi:10.1115/1.2803290
- 769 50. Li, J.; Li, J. C. M. Temperature distribution in workpiece during scratching and
770 grinding. *Mater. Sci. Eng.* **2005**, A 409, 108–119. doi:10.1016/j.msea.2005.07.057
- 771 51. Xu, X. Experimental study on temperatures and energy partition at the diamond-granite
772 interface in grinding. *Tribol. Int.* **2001**, 34, 419–426. doi:10.1016/S0301-
773 679X(01)00039-1
- 774 52. Malkin, S.; Guo, C. Thermal Analysis of Grinding. *CIRP Ann. - Manuf. Technol.* **2007**,
775 56, 760–782. doi:10.1016/j.cirp.2007.10.005
- 776 53. Vinay, P. V.; Rao, C. S. Influence of Process Parameters on Grinding - A Review. **2015**.
- 777 54. Doman, D. A.; Warkentin, A.; Bauer, R. Finite element modeling approaches in
778 grinding. *Int. J. Mach. Tools Manuf.* **2009**, 49, 109–116.
779 doi:10.1016/j.ijmachtools.2008.10.002
- 780 55. Wang, Y.; Chu, X.; Huang, Y.; Su, G.; Liu, D. Surface residual stress distribution for
781 face gear under grinding with a long-radius disk wheel. *Int J Mech Sci.* **2019**, 159, 260-
782 266. doi:10.1016/j.ijmecsci.2019.06.004
- 783 56. Guo, Y. B.; Barkey, M. E. FE-simulation of the effects of machining-induced residual
784 stress profile on rolling contact of hard machined components. *Int. J. Mech. Sci.* **2004**,
785 46, 371–388. doi:10.1016/j.ijmecsci.2004.03.014
- 786 57. Rami, A.; Kallel, A.; Djemaa, S.; Mabrouki, T.; Sghaier, S.; Hamdi, H. Numerical
787 assessment of residual stresses induced by combining turning-burnishing (CoTuB)
788 process of AISI 4140 steel using 3D simulation based on a mixed approach. *Int. J. Adv.*
789 *Manuf. Technol.* **2018**, 97, 1897–1912. doi:10.1007/s00170-018-2086-7

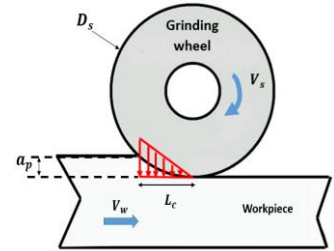
- 790 58. Sartkulvanich, P.; Altan, T.; Jasso, F.; Rodriguez, C. Finite Element Modeling of Hard
791 Roller Burnishing: An Analysis on the Effects of Process Parameters Upon Surface
792 Finish and Residual stresses. *J. Manuf. Sci. Eng.* **2007**, 129, 705–716.
793 doi:10.1115/1.2738121
- 794 59. Rami, A.; Kallel, A.; Sghaier, S.; Hamdi, H. Residual stresses computation induced by
795 turning of AISI 4140 steel using 3D simulation based on a mixed approach. *Int. J. Adv.*
796 *Manuf. Technol.* **2017**, 91, 3833–3850. doi: 10.1007/s00170-017-0047-1
- 797 60. Bhushan, B. *Introduction to tribology*. Wiley. **2002**.
- 798 61. Matsumoto, Y.; Magda, D.; Hoepfner, D. W.; Kim, T. Y. Effect of machining processes
799 on the fatigue strength of hardened AISI 4340 steel. *J. Manuf. Sci. Eng. Trans.* **1991**,
800 *ASME* 113, 154–159. doi:10.1115/1.2899672
- 801 62. Revankar, G. D.; Shetty, R.; Rao, S. S.; Gaitonde, V. N. Wear resistance enhancement
802 of titanium alloy (Ti-6Al-4V) by ball burnishing process. *J. Mater. Res. Technol.* **2017**,
803 6, 13–32. doi:10.1016/j.jmrt.2016.03.007
- 804 63. Ben Fathallah, B.; Dakhli, C. E.; Terres, M. A. The effect of grinding parameters and
805 gas nitriding depth on the grindability and surface integrity of AISI D2 tool steel. *Int. J.*
806 *Adv. Manuf. Technol.* **2019**, 104, 1449–1459. doi:10.1007/s00170-019-03943-4

Graphical abstract

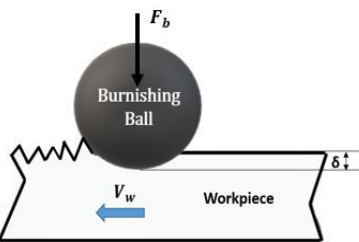
Yasmine Charfeddine

Experimental set-up

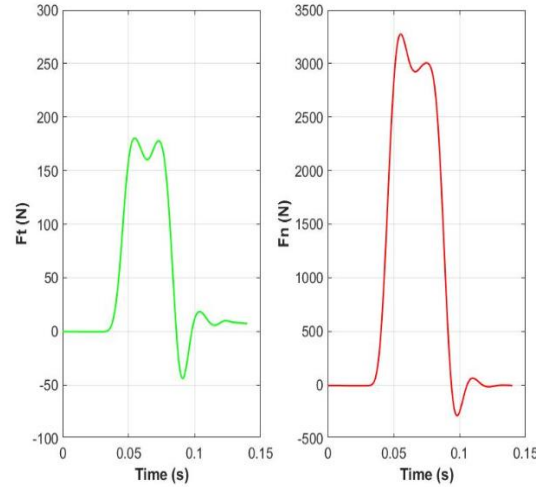
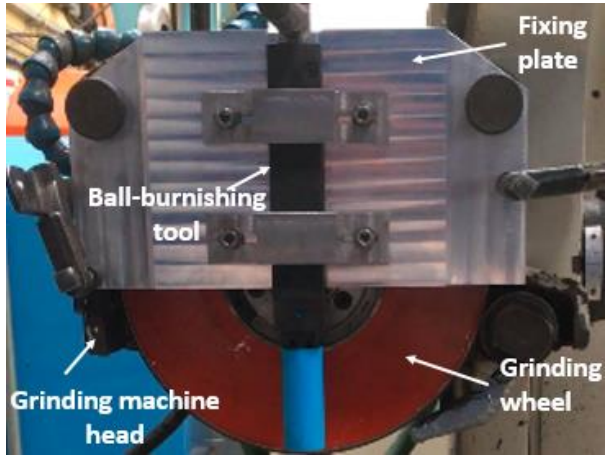
Grinding process



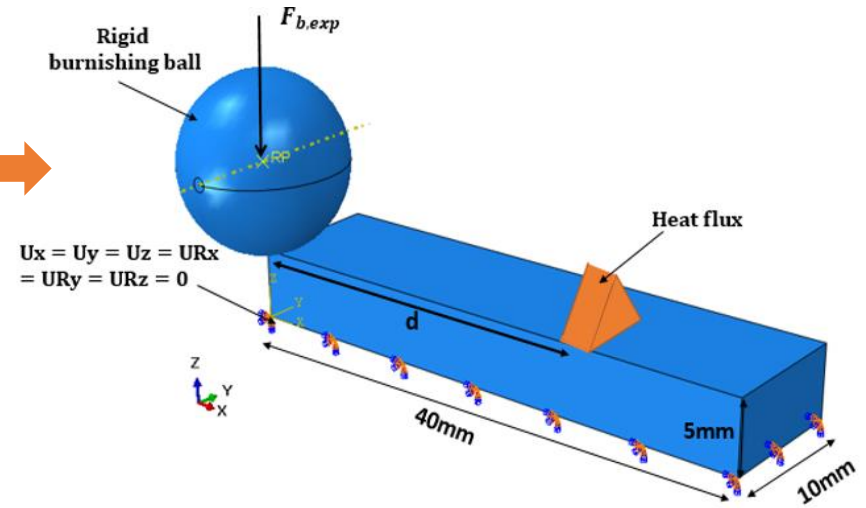
Ball-burnishing process



REGAL Hybrid process



Modelling & 3D FEM simulations

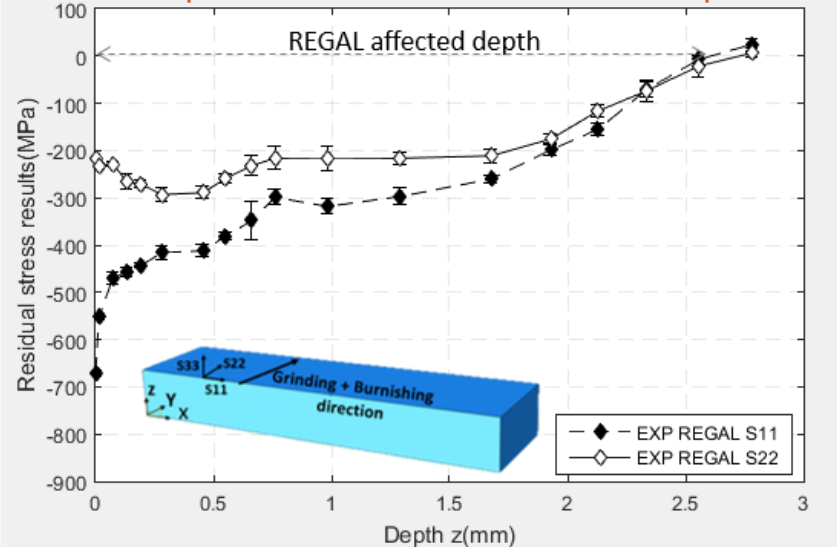


Combined process Grinding/Ball-Burnishing

Main results

- Thick Compressive Residual stress layer of about 2.7 mm
- High compressive residual stress level
- A threshold depth is reached for a threshold burnishing force
- Interesting functional surface that may surely improve lifetime in case of severe rolling contact or slip contact, for example

Experimental REGAL residual stress results vs depth



Numerical residual stress results vs depth

